




A review of selected small specimen test techniques for identifying deformation and failure properties of metallic materials

Xiaorui Wang¹, Tao Zhu^{1,*} , Jingke Zhang¹, Haoxu Ding¹, Shoune Xiao¹, Liantao Lu¹, Bing Yang¹, Guangwu Yang¹, and Yanwen Liu^{1,2}

¹State Key Laboratory of Traction Power, Southwest Jiaotong University, Chengdu, China

²Basic R&D Department, National Railway Passenger Car Engineering Research Center, Changchun Railway Vehicles Co., Ltd., Changchun, China

Received: 31 July 2022

Accepted: 11 November 2022

Published online:

19 November 2022

© The Author(s), under exclusive licence to Springer Science+Business Media, LLC, part of Springer Nature 2022

ABSTRACT

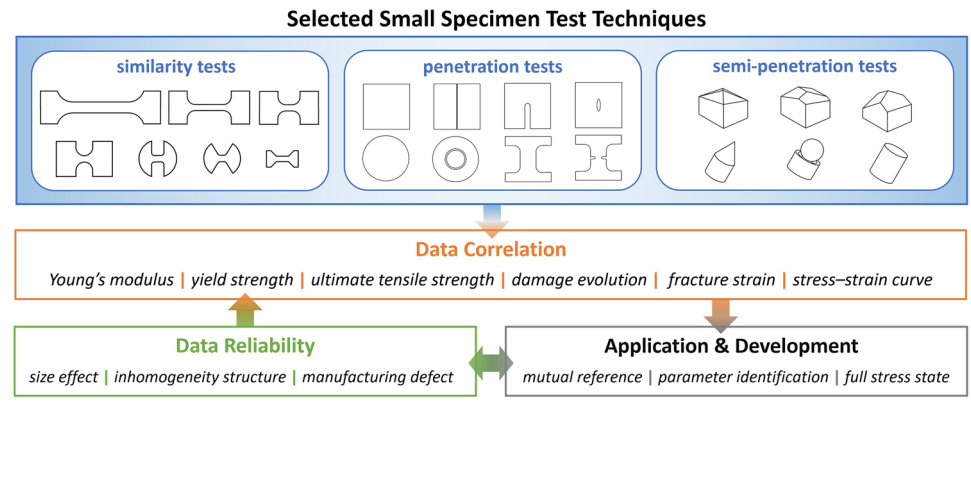
Small specimen test techniques (SSTTs), developed for scarce materials, industrial products, in-service equipment, etc., could be challenging to obtain sufficient materials for routine testing. This review focuses on the research on millimeter- and micron-scale SSTTs of metallic materials in the past decade. Mainstream small specimens are divided into similarity, penetration, and semi-penetration. Representative tests of the above three categories are analyzed in detail, including the small tensile test, small punch test, and indentation test. The macro- or micro-correlation methods of deformation and failure parameters between the SSTTs and conventional tests are discussed, including Young's modulus, yield strength, ultimate tensile strength, damage evolution, fracture strain, and the stress–strain full-history relationships. Meanwhile, the extensive requirements for material testing are also considered, such as anisotropy and strain rate, temperature, and stress triaxiality sensitivities. The characteristics and modification strategies of the SSTTs are described from the aspects of size effects, inhomogeneous structures, and manufacturing defects. Finally, this paper discusses the application of SSTTs in forging, stamping, welding, and additive manufacturing and highlights the potential development directions of SSTTs.

Handling Editor: Megumi Kawasaki.

Address correspondence to E-mail: zhutao034@swjtu.edu.cn

<https://doi.org/10.1007/s10853-022-07973-4>

GRAPHICAL ABSTRACT



WJ Welded joint

Abbreviations

AA	Aluminum alloy
AM	Additive manufacturing
CDM	Continuum damage mechanics
CSM	Continuous stiffness method
CTT	Conventional tensile test
DIC	Digital image correlation
DVC	Digital volume correlation
ECM	Expanding cavity model
EEP	Energy equivalence principle
FEA	Finite element analysis
GND	Geometrically necessary dislocation
GTN	Gurson–Tvergaard–Needleman
HAZ	Heat affected zone
IAF	Indenter area function
IESR	Indentation energy scale relationship
IT	Indentation test
SCT	Small compression test
SDE	Strength difference effect
SPT	Small punch test
SS	Stainless steel
SSD	Statistically stored dislocation
SSM	Single stiffness method
SSPT	Small shear punch test
SSTT	Small specimen test technique
STT	Small tensile test
UTIR	Ratio of unloading work to total indentation work
UTS	Ultimate tensile strength

Introduction

Small specimen test techniques (SSTTs) were first developed for the material testing of nuclear reactors, residual life assessment of in-service components, local property measurement in the welding industry, and mechanical property evaluation of miniature devices [1]. SSTTs can cover geometric feature sizes on the order of nanometers, microns, and millimeters (also known as nano, micro, meso, and macro). However, a consensus has yet to be reached on judging the critical size between small specimens and conventional specimens; a geometry more diminutive than the recommended range of the standard could be generally regarded as small specimens. The current application scenarios of SSTTs include aging monitoring of in-service equipment (e.g., nuclear energy, petroleum, and chemical industry); material testing with small size but high testing demand (e.g., nanomaterials, composites, and precious metals); research on local mechanical properties of inhomogeneous materials and structures (e.g., welding, stamping, and other complex components with narrow geometry); and analysis of microscopic or mesoscopic mechanical properties (e.g., micro-

electro-mechanical systems, gradient materials, and thin-film materials).

The small specimens preserved the same characteristics as the conventional specimens to ensure data comparability, shown in the following aspects. (a) Sufficient grains in the geometric feature size should ensure micro characteristics (grains, grain boundaries, second phases, inclusions, etc.) to present the macro mechanical properties of the material. (b) Stable deformation mode and stress state during loading (e.g., uniaxiality or multiaxiality, plane stress, or plane strain) to accurately reflect the behaviors under the expected stress states. (c) The geometric similarity of different specimens in similar tests makes measured parameters comparable. (d) A lower size limit shall ensure the interchangeability of various test devices and clamps.

According to the specimen's geometric shape and the test loading characteristics, SSTTs can be divided into similarity, penetration, and semi-penetration types. The similarity type refers to the proportional or non-proportional reduction of the specimen geometry relative to the standard specimen, without parameter conversion by complex correlations, including the small tensile test (STT) and small compression test (SCT). The penetration type refers to the external elastic or rigid loading body that gradually punches through the thin specimen, and the extracted load–displacement response could be correlated with the conventional test, which is similar to the macro-forming test, including small punch test (SPT), small shear punch test (SSPT), and small punch beam test. The semi-penetration type refers to the external elastic or rigid loading body gradually pressing into the thick specimen, and the load–displacement response could also be correlated with the conventional test, which is similar to the macro hardness test, also called the indentation test (IT).

Three aspects should be considered when conducting a complete SSTT. First, specimen sampling, geometry design, and device selection. The mechanical property affected zones caused by heat, scratches, extrusion, and other factors should be avoided during the sampling process. Most studies have been conducted from two perspectives: one is the influence of defects generated by processing on the measured data reliability, which will be discussed later in this paper; the other is the development of sampling equipment [2] and methods [3], and the further treatment strategy on the surface after sampling

[4, 5]. Second, data correlation analysis at the middle stage, which contains elastic parameters (Young's modulus), plastic parameters (yield strength and stress–strain relationship), and failure parameters (ultimate tensile strength (UTS), damage evolution, elongation, and fracture strain). The SSTTs achieve good consistency with the conventional tests [6]. Third, data reliability verification is performed at the final stage, including the various influences on size effects, inhomogeneous materials and components, and manufacturing defects of specimens and devices. These three parts jointly ensure the consistency, uniqueness, and robustness of the SSTT results.

This paper mainly discusses the typical and widely applicable tests in three SSTT categories: the similarity type selects STT, the penetration type selects SPT, and the semi-penetration type selects IT. The deformation and failure behaviors of metallic materials identified by SSTTs are summarized, including the data correlation method of Young's modulus, yield strength, UTS, damage evolution, fracture strain, full-history stress–strain curve, and other parameters and responses. The extensive requirements of material testing, such as anisotropy, strain rate, temperature, and stress triaxiality sensitivities, are also discussed for the test devices, specimen geometries, and data processing methods. The characteristics and modification strategies of various SSTTs are expounded from the aspects of the size effect, inhomogeneous structure, and manufacturing defects. Subsequently, the engineering application status of various SSTTs is introduced. The advantages and limitations of various SSTTs are dialectically analyzed, and further development of SSTTs in testing the deformation and failure properties of metallic materials is investigated.

Test of similarity type

Configuration of STT

Background

The origin of the similarity type conforms to the inertia of scientific and technological development, which presents the proportional or non-proportional scaling of standard specimens. Hence, the geometric dimensions and test methods are similar to the conventional tensile test (CTT). The most commonly

used similarity type is the STT, also known as the micro/sub-size tensile test. Because of the simplicities of the geometric dimension and stress state under the uniaxial tensile state, the specific STT standard has yet to be published and implemented. The specimen geometries generally refer to CTT standards, such as ISO 6892-1 [7], ASTM E8 [8], and GB/T 228.1 [9]. STT specimens that fully inherit the geometric proportional relationship are classified as the strict similarity type, whereas others are classified as the relaxed similarity type. The test conditions under various temperatures, strain rates, and environments also refer to the corresponding standards. Furthermore, the loading mode, test device, and data processing method are also basically consistent with the above standards. The curve measured by the STT is in good agreement with the CTT, including evident stages of elasticity, plasticity, and softening.

Geometry

Several basic principles should be followed in the geometric design of the STT specimens [10]. (a) The specimen geometry should reproduce a polycrystalline-like behavior, containing at least 5–6 grains per smallest dimension. The typical grain size for ferrous and non-ferrous alloys is approximately 40–50 μm , resulting in 300–400 μm being the limiting minimum thickness for the specimen. (b) To accurately reproduce necking and strain localization behaviors, the geometry should satisfy specific thickness/width and length/cross section requirements. (c) The specimen geometry is simple and avoids or minimizes rounded shapes to reduce the sample production cost.

The mainstream STT specimens also have flat and round shapes, such as CTT, and the typical STT geometric appearance is shown in Fig. 1. Both flat and round specimens can better reflect the mechanical properties of the materials [11]. However, the round specimen has difficulty in manufacturing and matching the test device and measuring equipment [12], resulting in it being rarely used [13]. Inheriting the standards or other reasonable dimensional relationships is key to the accuracy of the results, whether flat or round specimens [14, 15]. For the gauge profiles, Cruz et al. [16] found that the plastic flow behavior of the material before softening can be well-described whether the gauge shape presents as a straight line or an arc. Liu et al. [17] proposed that the influence on the measured results gradually decreased and then increased with the reduction in the gauge length; therefore, an optimal size can be found. At the same time, the specimen reflects a higher bending stiffness caused by the reduction in gauge length, which could be more convenient for manufacturing and testing. Hwang [4] suggested that a larger gauge diameter can be used as much as possible for round specimens to reduce the surface effect and test error. Yuan et al. [18] discussed the difference in necking with different gauge diameters and found that the diameters were independent of the UTS, area reduction, and elongation. The deformation length after necking depended only on the gauge diameter and not on the gauge distance. The size dependence of the tensile properties can be eliminated when the length-to-diameter ratio is greater than 10. Similar results were obtained for the flat shape (gauge thickness of not less than 1 mm), and the thickness of the specimen only affected the

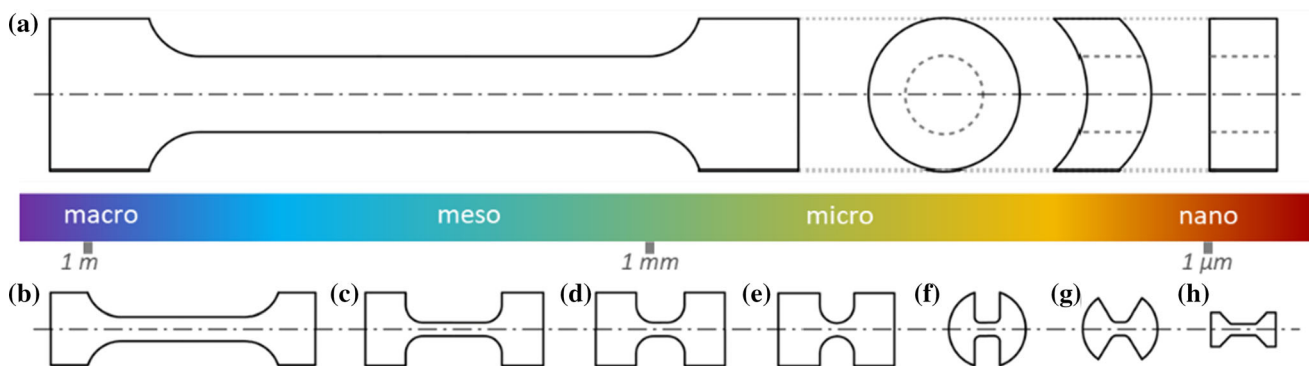


Figure 1 Geometries of various STT specimens (list from large to small). **a** Dog bone (round, curved and flat shapes), macroscopic standard [7–9]. **b** Dog bone, proportion [7–9, 21]. **c** Dog bone,

non-proportion [16]. **d** Dog bone, short gauge [16]. **e** Dog bone, arc gauge [12]. **f** Small disc [25]. **g** Ultra-small disc [25]. **h** Bow tie [10].

elongation after necking [19]. For the dimension of the transition section, Bergonzi et al. [20] considered the influence of the stress concentration degree and contact force distribution (different contact points between the specimen and clamp owing to different radii) on the test results and determined the optimal size of the transition arc between the head and the parallel section of the specimens. The STT is also applicable to curved surface specimens sampled from tubular components, and the characteristics of the test results are similar to those of curved surface CTT [21]. In addition, several ingenious geometric designs have been considered [22]. With a further reduction in specimen size, measurement uncertainties increase; hence, a sufficient number of specimens is required to complete the statistical measures of uncertainty [23]. Considering the microstructure, size effect, manufacturing accuracy, and other issues of the STT specimens comprehensively, some size restrictions can be proposed for the meso-scale STT specimens to guide design. For round specimens, the manufacturing accuracy should be considered when the gauge length is less than 5 mm [4]; the gauge length and diameter are generally at least 1 mm [13]. For flat specimens, the ratio of thickness to grain size should not be less than 5–10 [10], generally not less than 1 mm [19], and the minimum is 0.2 mm [24]; the gauge length less than 2 mm will lead data scattering [17]. The transition arc should not be too small compared to the gauge dimensions to avoid the wrong stress and strain states [20].

Test device

The STT test device system includes frame equipment (mainly clamps) and measuring equipment (mainly measuring the displacement or strain fields). Commonly used displacement or strain measuring equipment includes contact and non-contact extensometers, such as small mechanical extensometers, laser extensometers, digital image correlation (DIC) systems, line scan cameras, and relative displacement of inter-particles in the microscope view field [26]. It is difficult to clamp or glue the traditional mechanical extensometers directly onto the small specimen surface, while the extension directly obtained between clamps includes the deformation of the loading frame and specimen shoulder. The DIC method can conveniently measure the strain field of the arc section and head of specimens; hence, it is widely used in STT. The traditional

speckle spray method can only provide medium-density speckles, whereas speckles of 3–7 pixels provide the best sensitivity and the slightest error [10]. In addition to the spray method, Nozawa et al. [27] proposed a non-painting DIC method that exploited the surface defect characteristics of a specimen, circumventing the difficulty of spraying fine speckles in STT specimens. The machining accuracy and alignment of the clamped components (the concentricity of the clamping force and load direction) were also considered. When the specimen bears an eccentric load, the stress distribution on both sides of the specimen axis is inhomogeneous, the ductile metals first yield on the side with large stress, and the brittle metals may fracture earlier, which leads to significant errors or even wrong results [14]. The design and development of STT centering test devices suitable for various geometric shapes are vital to ensuring the reliability of the measured data [16]. Less attention has been paid to the deformation and failure characteristics of materials under different stress states (stress triaxiality and Lode parameter) in specimens with different notches, although such research is highly active in CTT. With the development of SSTTs, the importance of this type of research in STT has become significant concerning the constitutive, damage, and fracture behaviors under full stress states and wide strain rates, which could be more in line with the actual needs of engineering structures. It is necessary to ensure that the stress triaxiality and average strain rate remain unchanged during STT. The constant stress triaxiality maintains the monotonous loading path (i.e., load history independent), and the constant average strain rate ensures a negligible effect on the strain rate sensitivity. According to the existing literature, the change in stress triaxiality depends on the design of the specimen shape and the hardening ability of the material, and the average strain rate can be maintained by changing the loading rate of the test devices [28], which should be considered in the design and development of specimens and devices in future.

Data correlation of STT

Elastic parameter

The measurement of Young's modulus in STT is usually unsatisfactory, which is attributed to the single or joint influence of material sampling, the manufacturing process of specimens, dimensional

relationships of geometries, alignment of loading frames, and compliance of test devices [15]. Consistent with the CTT calculation method, Young's modulus, defined as the slope of the elastic stage in the stress–strain curve, explicitly reflects the accurate measurement of force and displacement. The influence of the force level mainly originates from the poor alignment of the loading frames or manufacturing defects of the specimens. Meanwhile, selecting different clamping positions, such as the gripping section, transition section, and gauge section, also affects the accuracy of Young's modulus. Because the manufacturing inhomogeneity of the transition section affects the overall force level and even leads to premature fracture, Young's modulus obtained by clamping only the gauge section could be the most accurate [29]. Venkatachalam et al. [30] discussed the sensitivity of the cross-sectional area of the gauge section to Young's modulus using the DIC method and found that the influence of the cross-sectional area was more significant than the axial length of the gauge section, and a small cross-sectional area would magnify the influence of defects. Ma et al. [31] indicated that the horizontal-type layout of test devices in STT would lead to the overturn of the clamps and further affect the measurement of the actual displacement, and then established modified equations considering the overturning moment, bending moment, and geometric relationship. The deformation of the non-gauge section and loading frame most derives the displacement measurement error. Hajy Akbary et al. [32] reported that Young's modulus can be jointly affected by the arc section's elongation and the test frame's compliance and proposed a load function of the fillet elongation and the test device compliance. They subtracted this term from the crosshead displacement, resulting in a reliable Young's modulus. Yang et al. [33] found that the deformation of the non-gauge section only accounted for a small part of the measurement deviation, and most of the deviation was caused by the compliance of the test devices. However, the measured Young's modulus still had a particular gap compared with that measured by the CTT. In addition, a series of methods, such as the energy method, can be used to measure Young's modulus. Zhang et al. [13] conducted STT on flat and round specimens and proposed a semi-analytical model to solve the load–displacement curve based on the assumption of energy equivalence, which could accurately measure Young's modulus.

Plastic parameter

The plastic parameters include yield strength, hardening exponent, and the stress–strain relationship can be obtained directly from STT. The solution method for various plastic parameters still inherits the methods in CTT (e.g., 0.2% offset solving for yield stress, logarithmic conversion between true and engineering curve). The test results of the STT are suggested for comparison with the CTT to verify the accuracy of the plastic parameters after eliminating the interference factors [3, 21, 23]. DIC is an effective method for identifying the strain field, especially in test scenarios that do not recommend contact, such as evaluating irradiated materials [34]. McClintock et al. [35] studied the effect of irradiation on the material microstructure and the changes in the constitutive relationship, elongation, and fracture mechanism. Gussev et al. [36] studied the accurate description of face-centered cubic metals' stress–strain relationship and discussed the effects of damage dose, temperature, and grain size on the constitutive equation without considering the large plastic deformation. Kamaya et al. [37] measured the stress–strain curve of stainless steel (SS) 316L and found that both DIC and mechanical extensometer methods could obtain consistent results, whereas the curve after necking was identified by iterative finite element analysis (FEA). McClintock et al. [38] indicated the inhomogeneity of the deformation and strain field, which occurred as a hotspot phenomenon of localized strain and deformation bands. The deformation bands propagated during the test and either fully or partially traversed the gauge section as deformation waves, which could explain the decreased load after yielding. The strain rate was homogeneously distributed over the gauge section in the hardening stage. Rund et al. [39] found that STT can be achieved at a lower loading rate than CTT under an expected strain rate, which could significantly reduce the common problems of oscillations under high strain rates and maintain high consistency.

Failure parameter

In general, SSTTs exhibit great scattering in predicting failure parameters (especially post-necking behavior) [33]. STT specimens are more difficult to process than SPT and IT specimens, but the measured data can be used directly [40]. Zhang et al. [41]

indicated that aluminum alloy (AA) had little dependence on specimen size before necking, whereas after necking, a difference may be caused by geometric instability and the distribution of micro defects. Scattering makes it difficult to obtain the fracture strain by inverse FEA, and the repeatability of the fracture strain identified by DIC also needs to be further studied. Many studies have focused on the influence of gauge dimensions on necking and softening and have regarded an increase in total elongation with a decrease in gauge length as a common phenomenon [15]. Kumar et al. [42] proposed that the reason for the continuous increase in the total elongation in higher thickness STT was that sufficient volume in the gauge section could maintain elongation and resist fracture. Lall et al. [43] indicated that the effect of thickness was essentially the effect of the number of grains in the thickness direction by in situ STT. The yield strength was stable on sufficient grains, whereas the necking mechanism was different. After the UTS, the shear failure and diagonal localized necking occurred in the thinner specimens. However, thicker specimens triggered diffusion necking, the shear failure area at the edge decreased, and the dimpled area of the specimen center increased, indicating the formation of conjugated localized shear bands on the upper and lower surfaces. Yang et al. [33] pointed out that the stress states of specimens in CTT and STT were the same in the elongation stage, while after necking, different fracture mechanisms led to different ductility's. A subsequent study of welded joints (WJs) obtained similar conclusions, which reflected different fracture positions in the CTT and STT. The difference in geometric dimensions led to a difference in the degree of constraint; hence, the fracture initiation position changed accordingly [44]. A potential research direction is failure behaviors under wide strain rates and various stress states, which have been relatively active in CTT. Sun et al. [45] combined SHPB for impact STT and found that the specimen with a short gauge had the most significant elongation after a fracture. They considered the elongation after a fracture as a fracture-strain-related parameter and then coupled the element size effect to the dynamic impact and collision problems. Notched specimens can be used to study stress triaxiality sensitivity. Arnaud et al. [46] pointed out that notched specimens could reflect fracture information to a certain extent despite the sensitivity of manufacturing defects, providing a

feasible idea for obtaining fracture strain under various stress states in STT (Table 1). Because the size of the STT specimen is relatively small, a design with a reasonable geometric size that can produce homogeneous strain and stress triaxiality fields during STT becomes an important issue. Even for uniaxial tensile specimens, the field variable distribution of SST is inferior to that of CTT [26]. The specimen size and material mechanical properties cause different restraint degrees of notched or non-notched STT and CTT specimens, which present different distributions of stress triaxiality fields and affect the accurate judgment of plasticity and failure [23]. Furthermore, the evolution mechanism of the microstructure can also provide theoretical support for the damage evolution and fracture mode of materials [47].

Data reliability of STT

Size effect

The size effect can be divided into two types: one is the deviation of the test data caused by the specimen size deviating from the standard; at this moment, the STT specimen could still reflect the macro behavior of materials from the perspective of continuum mechanics, and the other is the ultra-small specimen size that is unable to reflect the macro behavior of materials [48]. A consensus could be that a homogeneous structure with at least six to 10 grains or 200–500 microstructural features within the deformation section [23] and the yield strength and UTS sensitivities could be different [49]. Wharry et al. [50] indicated that the difference in specimen size led to a change in the deformation mechanism, which contained fewer dislocation sources; hence, plastic yielding could not occur until a sufficient population of dislocations was introduced into the specimen from external loading, resulting in the measured yield strength exceeding the CTT value and approaching the theoretical strength. When the specimen size increased to the transition dimension, the yield strength was independent of the specimen size, referring to abundant dislocation sources within the specimen volume. The transition dimension is inherently correlated with the material microstructure, and this relationship is significant for SSTTs. In terms of statistical theory, the grain size effect is greater than the inherent size effect; the size effect intensity on compression strength is more significant

Table 1 Representative methods and formulas of STT data correlation

Type	Parameters	Methods	Formulas	References
Elasticity	Young's modulus	Extensometer or DIC	$E = \Delta R / \Delta e$	[7–9]
		Elastic strain correction	$\varepsilon_{\text{mod}}^e = (\Delta L_a - \Delta L_m) / (L_p + 2\eta L_p)$	[32]
Plasticity	Yield strength	0.2% offset strain method	$\sigma_y(\varepsilon_{\text{en}}) = E(\varepsilon_{\text{en}} - 0.2\%)$	[7–9]
	Full-history	Logarithmic transformation	$\sigma = \sigma_{\text{en}}(1 + \varepsilon_{\text{en}})$, $\varepsilon = \ln(1 + \varepsilon_{\text{en}})$	[7–9]
Failure	UTS	Maximum stress	$\sigma_u = \max[\sigma_{\text{en}}]$	[7–9]
	Damage	Apparent elastic modulus	$D = 1 - \tilde{A} / A_0$	[17]
	Elongation	Standard method	$A = \Delta L / L$	[7–9]
	Fracture strain	Cross section method	$\varepsilon_f = \ln(A_0 / A_f)$	[40]

where E is Young's modulus; σ and σ_{en} are true stress and engineering stress; σ_y and σ_u are yield strength and UTS; A is elongation; D is damage; ε , ε_{en} and ε_f are true, engineering and fracture strains; $\varepsilon_{\text{mod}}^e$ is the modified elastic strain considering deformation out of gauge; \tilde{A} , A_0 and A_f are effective, initial and fracture area of cross section; ΔR is stress difference in Δe interval; Δe is elastic strain difference in a specified interval; L is initial gauge length; ΔL , ΔL_a , ΔL_m and ΔL_p are gauge, apparent, machine and parallel-section elongations; η is coefficient

than tensile strength when considering the strength difference effect (SDE) [51]. Yalçinkaya et al. [52] studied microstructures with different numbers of grains with random orientations and investigated the influence of the grain size and number on both the local and macro behaviors of materials. Zhu et al. [53] combined SHTB with STT and studied the influence of the size effect on the deformation behavior of pure titanium foil with different grain sizes. The microstructure evolution mechanism under a high strain rate (above 1000/s) was significantly different, and the fracture mechanism changed from the mixed fracture mode of ductile fracture and cleavage fracture to pure ductile fracture.

Inhomogeneity structure

The inhomogeneous structural gradient and particles of the STT specimens could affect the test results. Ando et al. [54] found significant differences in the STT results between micron and millimeter specimens sampled at different locations owing to the inhomogeneous structure. Based on the sufficient number of grains in STT specimens (without the size effect), Xu et al. [55] found that inclusion in the matrix would not affect the hardening ability of materials but would reduce the ductility, providing a reference for material toughening. Kumar et al. [42] studied the minimum material volume in the gauge section to be comparable between the STT and CTT curves and found that non-uniform deformation occurred when the thickness of the specimen was less

than 0.3 mm. The selection of thickness should be cautiously considered. For thick specimens, the specimen had sufficient volume in the gauge section to maintain elongation and resist fracture, indicating that the shear fracture mechanism mainly existed. For thin specimens, the void initiation and coalescence mechanisms mainly existed, and the non-uniform deformation of the specimens resulted in the rapid evolution of voids, reduction of elongation, and premature fracture. The Ashby's model can further explain the low strength of thinner specimens. In CTT, the grains of a polycrystalline material constrained each other to accommodate the misfit between them in the form of geometrically necessary dislocations (GNDs), which induced a wide range of back-stress fields. The internal crystal in thick specimens generated back-stress to resist the tensile force, and the relaxed back-stress reduced the yield strength and UTS of the thin specimens [2].

Manufacturing defect

Appropriate sampling and processing methods are required to ensure the surface quality (i.e., roughness and flatness), internal defect ratio, and geometric symmetry of specimens, and maintaining the accuracy and robustness of the mechanical properties of materials are vital issues [3, 56]. Arnaud et al. [46] found that the nano-roughness caused by the manufacturing defects of a focused ion beam had a particular impact on micron specimens. Dzugan et al. [57] performed STTs with different sampling

positions, sampling directions, and thicknesses for two types of additive manufacturing (AM) specimens: selective laser melting and selective electron beam melting. Different surface qualities resulted in a significant scattering of Young's modulus and strength. The build orientation determined the microstructure and mechanical properties rather than the thickness and position within the build chamber. Liu et al. [17] found that the thinner specimens caused significant scattering, and the influence of inhomogeneous thickness became significant. Deviation, waviness, roughness, etc., jointly determined the manufacturing inhomogeneity of the surface profile. Surface treatments can improve scattering. Caution should be exercised in the surface treatment process because the residual stress and residual deformation caused by mechanical extrusion, sliding, and heat sources would also deteriorate the scattering [58]. In addition, the material microstructure and structural integrity differ under various manufacturing processes. The difference in size, location, and number of defects could cause differences and instability in the mechanical properties [57]. Kale et al. [59] analyzed the non-uniform deformation of AM SS316L with different selective laser melting energy densities. The inhomogeneous microstructure leads to a non-uniform distribution of mechanical properties along the specimen, affecting the elongation, fracture strain, and fracture mode. Fang et al. [60] discussed the anisotropic plasticity and fracture behaviors and found that the influence of surface defects on ductility was greater than that of internal defects. Benzing et al. [61] discussed the effects of internal porosity, anisotropy, and microstructural inhomogeneity in the AM process and proposed a specimen size insensitive to the above factors.

Engineering application of STT

Millimeter-scale STTs are widely used in defect detection of micro components and local mechanical property testing of WJs [62]. Sridharan et al. [63] performed STT on ultrasonic AM AA6061 and found that the coalescence of pre-existing shear bands at the interfaces promoted the anisotropy of plasticity and fracture. Luo and Zhang [64] studied the constitutive relationship of the fusion zone of spot WJs and found that the microstructural defects and residual deformation produced by the manufacturing process can be intuitively observed from the non-uniform and

asymmetric strain field by DIC. Manikandan et al. [65] performed STT on AA2219-T87 friction stir WJs and investigated local regions' anisotropy and temperature sensitivity, reflecting the difference in the microstructure evolution mechanism. Therefore, studying the mechanical properties of WJs in local zones is necessary. However, sampling has significant limitations in the heat affected zone (HAZ) that could be narrow or inclined due to the groove. The isotropic material could ensure sufficient HAZ in the gauge section [66].

For structures with apparent differences in mechanical properties, such as WJs, a CTT with the sub-regional DIC method on whole joints could measure the mechanical properties of the local zone [67]. It is a generalized STT method; the same implies a small gauge length rather than a small specimen. Ambriz et al. [68] and Suthar et al. [69] studied AA6061 and AA6061-AA7075 friction stir WJs and observed non-uniform deformation caused by the difference in the stiffness of each area; the HAZ first significantly softened and failed. Furthermore, the digital volume correlation (DVC, namely 3D-DIC) method could concurrently measure the strain field of the front and side surfaces, making it more suitable for non-uniform specimen dimension [70], the stress–strain curve after necking, and anisotropy [71]. The DVC and DIC methods can also guide the zone division of WJs, which could better identify the zoning boundaries of WJs of all weld matching types (i.e., match, overmatch, and undermatch) [72]. The objective evaluation of generalized STT has been shown in Table 2.

Innovation of similarity test

In addition to the mainstream STT, tests of similarity type also include SCT [73], small three-bending test [74], small cantilever-bending test [75], small ring tensile test [76], small ring compression test [77], small disk bending test [23] (SPT has been developed on this basis, which will be discussed in detail in the subsequent section), small compact tensile test [25], small Charpy test [78], etc. The specimen shape can be standard, wire, disc, hourglass, or other variants [25]. SCT is generally used at the nano-scale, and in situ SEM observations are generally used to study localized deformation and orientation-dependent mechanisms [79]. Rovaris et al. [80] found the sensitivity of the specimen end face's curvature (surface

Table 2 Objective evaluation of the generalized STT

Progressiveness	Limitation
Convenient sampling, less processing, and more suitable for narrow substructure	The specimen is directly sampled from the engineering structure, and the material composition may change along the thickness direction (the transition of materials in the internal space of the specimen cannot be observed)
The stiffness of the specimen is larger than that of the specimen in the STT, which is difficult to buckle and insensitive to the alignment of the test devices	Large deformation and necking would occur in the local area with weaker stiffness; hence, the other zones would deform slightly, and a full-history curve cannot be obtained
The zone division can be adjusted based on the distribution of the strain field after the test with high adaptability	The uniaxial stress state cannot always be maintained because of the significant cross-sectional difference after necking, making it challenging to design specimens under various stress states
The order of magnitude of the test data is higher than that of the STT, and both instrumental and rounding errors are relatively small	Cannot obtain the fracture strains of all zones

inhomogeneity) in SCT, which caused stress inhomogeneity and changed the microstructure evolution mechanism. Jedrasiak and Shercliff [81] observed classic barreling and dead metal zones around clamps under various temperatures and strain rates. Kitamura and Terano [82] proposed a cubic SCT, considering the phenomenon of the specimen section evolving from square to rectangle, which could be suitable for identifying anisotropy. Mueller et al. [83] held that the error was mainly caused by deviations of the indenter placement point from the beam span center in the small three-bending test. Armstrong et al. [84] found that small cantilever-bending test could better reflect the ductility and brittleness of local zones than IT. The manufacturing problems mentioned above also affect the material's mechanical properties for these similarity type tests [85].

Test of penetration type

Configuration of SPT

Background

The inspiration for the penetration test comes from the conventional metal forming test, defined as an external elastic or rigid punch invading a flat specimen with a fixed boundary, causing the deformation and failure of the specimen. The penetration test is also a similarity type of conventional forming test from another point of view. Based on theoretical frameworks or inverse FEA, the correlation of

elastoplasticity and failure parameters between the penetration test and the CTT can be obtained. The SPT is the most active penetration test. Recently, SPT standards have been released, such as ASTM E3205 [86], EN 10371 [87], and GB/T 29459 [88]. The punch has ball and semi-ball shapes, as shown in Fig. 2a, which do not contribute to the test results because of the continuous contact between the punch's lower surface and specimen during SPT. The punch is generally selected as a ball shape, meeting the interchangeability requirement to prevent the cumulative damage from affecting the subsequent tests [89]. The typical responses of ductility and brittleness are shown in Fig. 2c and are mainly divided into five stages.

Stage I: linear-elastic bending, and the deformation of the specimen is controlled by Young's modulus and Poisson's ratio. Stage II: plastic bending, and the slope of the curve changes owing to the yield. Stage III: membrane stretching, and the specimen further deformed due to biaxial stress. Stage IV: plastic instability, and specimen thinning with the initiation and aggregation of voids. Stage V represents failure, and the crack begins to expand. In some studies, Stage V divides into two sub-stages: the crack initiation stage (V) and the bearing capacity complete loss stage (VI), which could better investigate the softening phenomenon of materials in the failure process. However, with the deepening of research, it has been found that Stage I is accompanied by elastic bending and plastic indentation [90], and the subsequent stages exhibit a non-uniform deformation with a

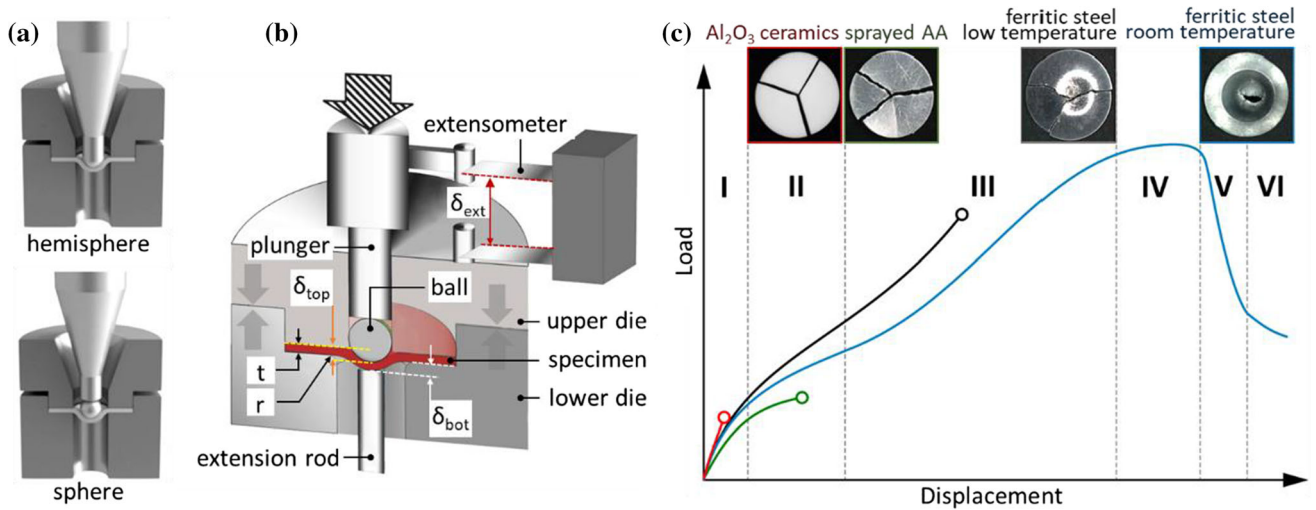


Figure 2 Configuration and general response in SPT. **a** Semi-ball and ball punch common used [87]. **b** Test system and displacement measurement methods [93]. **c** Typical force–displacement curves [94].

small amount of elastic deformation [91]. Plastic instability may occur before reaching the maximum load [92]. Therefore, the accuracy of the measured data and the necessity for strict reanalysis should be further discussed.

Geometry

SPT specimens are divided into round and square according to the outer contour; flat and tubular according to the straightness [95]; and standard, dog bone, and notch types according to the inner contour [90], shown in Fig. 3. Notched specimens are mostly used to measure the fracture toughness and ductile–brittle transition temperature. The recommended thickness of the SPT specimen is 0.5 mm [86–88], and whether thinner specimens can be used is also a controversial issue. Haroush et al. [96] and Priel et al. [97] studied SS316L thin foils and found that a thickness of 300–500 μm still satisfied the thin plate bending equations; a thickness below 50 μm should

employ the equations derived from the membrane solution rather than classical plate theory; and a thickness of 50–300 μm belonged to a transition zone between the plate and membrane states. For the length or diameter, it is generally selected within two ranges specified in the standards; that is, for the measurements of macro mechanical behaviors select 8–10 mm; for the materials requiring microstructure observation select 3 mm [86–88]. Simonovski et al. [95] conducted SPTs of rectangular, circular, and tubular specimens and found that the results of rectangular and circular specimens were consistent; the maximum loads of tubular specimens were slightly larger, while the maximum displacements were slightly smaller. The curved surface shape affected the friction; hence, different clamping degrees led to a deviation in the measured yield strength. Some innovative designs, such as dog bone SPT specimens, can place the specimens in a uniaxial stress state during loading [90]. This type of specimen provides an idea to carry out SPT under a specific

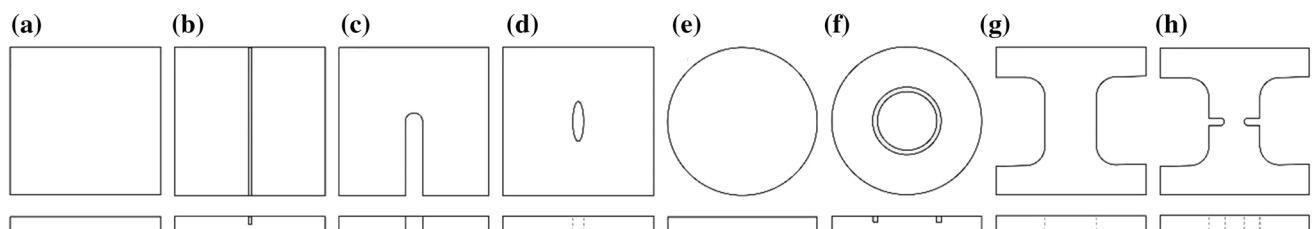


Figure 3 Geometries of various SPT specimens. **a** Rectangle, standard [90]. **b** Rectangle, surface notch [98]. **c** Rectangle, through-thickness notch [99]. **d** Rectangle, central notch [89].

e Circular, standard [87]. **f** Circular, surface ring notch [100]. **g** Dog bone, standard [90]. **h** Dog bone, through-thickness notch [101].

stress triaxiality, breaking through the lack of theories to study the correlation between the biaxial response of SPT and the uniaxial response of CTT, making it possible to obtain the deformation and failure behaviors under full stress states in SPT.

Test device

Research on the SPT system focuses on the setting and coordination of the test frame and accurate measurement of displacement. Different parameter settings are essential factors that affect the SPT results. For instance, the thickness of the specimen, diameter of the ball punch, fillet of the lower die, and chamfer would affect the value of the contact reaction force, which affects the SPT response [102]. A possible internal reason is that the microstructural evolution mechanism changes under different parameters in each loading stage, causing a change in the SPT curve [102]. The gap between the ball and the lower die generally follows the standards [86–88], and different gaps place the specimen in different stress states [103]. Rasche and Kuna [94] held that the clamping force falsified the measurements for brittle materials; omitting the lower die and expounding the integrated punch was more suitable for the SPT of brittle materials. Researchers have different views regarding the use of upper dies. Andrés and Dymáček [104] analyzed different upper die clamping conditions (i.e., displacement constraint, force constraint, no gap, and no upper die) and found that the clamping conditions of the upper die had little effect on the measured mechanical properties, while the measurement of yield strength and UTS would be low without the upper die. Therefore, the upper die is recommended, which also makes the SPT under the condition of shallow indentations feasible. The clamping force setting is also a factor to be discussed. A clamping force that is too small will lead to sliding between the clamp and the specimen, and a clamping force that is too large will cause irreversible deformation of the specimen. Simultaneously, the clamping force affected the amplitude and growth rate of the load to a certain extent [105]. The friction coefficient significantly influences the stage from plastic instability to failure and even affects the fracture position of the specimen. Friction restrains the pull-off phenomenon of specimens between the upper and lower dies; hence, the homogeneity of friction is also a key issue in ensuring the reliability of the SPT [102, 106].

For accurate displacement measurement without considering the compliance of test devices, linear variable displacement transducers and crack opening displacement extensometers are commonly used [89]. Sánchez-Ávila et al. [107] proposed a method of continuous loading–unloading to separate the responses of elastic and plastic deformation and an obtained accurate displacement expression. Different definitions of displacement also have a significant impact on SPT results. Moreno et al. [93] compared the differences between three displacement definitions: the displacement of the loading frame relative to the upper die, the displacement of the ball, and the deflection at the bottom of the specimen, as shown in Fig. 2b. The displacement defined at the bottom of the specimen presented the actual displacement of the specimen, excluding extra contributions due to neither the deformation of the intermediate kinematic chains nor the ball indentation during the test. Some methods without mechanical measurement exist. Vijayanand et al. [108] set a 45° inclined mirror and built a macroscopic in situ DIC system. In this case, DIC only identified the out-of-plane deformation, which put forward stricter requirements for identification technology, and the DVC method may be an appropriate choice. The non-contact measurement is applicable to impact SPT because the mechanical extensometer can be damaged during impact loading. The impact SPT system can consist of an SHPB or drop-weight testing machine [109, 110].

Data correlation of SPT

Elastic parameter

The solution of Young's modulus includes the Stage I slope and unloading slope methods, establishing the relationship between Young's modulus and slope, specimen thickness, Poisson's ratio, and other parameters [90, 105]. However, Stage I includes the plastic indentation and elastic bending of specimens, which cannot be strictly regarded as pure elastic deformation; Stage II includes the plastic deformation under the punch and the elastic bending of the surrounding materials, which cannot be strictly regarded as the pure plastic deformation [91]. In contrast, unloading is pure elasticity and Poisson's ratio independent and is a feasible method to establish the relationship between the unloading slope and Young's modulus without considering the damage

evolution [111]. To avoid the limitation of low Young’s modulus measured by the Stage I slope method, Chica et al. [112] introduced the unloading/loading cycle to solve the mapping coefficient of Young’s modulus, which applied to most isotropic and homogeneous metals and only related to specimen geometries.

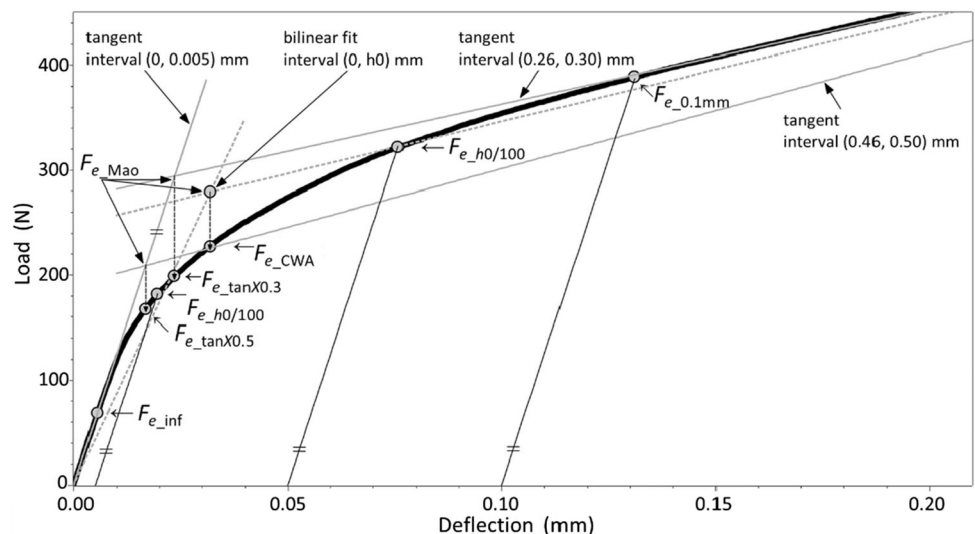
Plastic parameter

The determination of the yield point in the SPT curve usually involves determining the elastic–plastic transition force F_e , which is mapped to the yield strength $R_{p0.2}$ in the CTT stress–strain curve. Standard solution methods include the two-line, offset, and inflection point methods, as shown in Fig. 4. The selection of two lines has been widely discussed, divided into the bilinear method and the two-tangent method with the development of research [113]. The bilinear method fits two connected lines in a specified continuous interval and ensures the least mean squares. In contrast, the two-tangent method solves the tangent in the specified discrete interval. The interval selection of the bilinear method has a recommended value in standards, called the specimen thickness h_0 (also the CEN or CWA method) [87]. The two-tangent method has no standard for providing a basis for selecting intervals. The above two-line methods are defined based on the load–deflection curve. For the load–displacement curve, the three-line method should be introduced to correct the influence of compliance [87]. The offset method was inspired by the 0.2% strain offset method based on

the elastic line in the CTT to determine the yield stress. The offset datum selects the tangent passing through the coordinate origin or fitting line in a specified interval in Stage I. The offset distance mainly includes thickness-related $h_0/10$ or $h_0/100$ and an independent 0.1 mm fixed-point strategy [114, 115]. The inflection point method is similar to the inflection point of the yield strength in bilinear elastoplastic materials; the point deviating from the above initial tangent or fitting line refers to the yield point [114].

Although a deformation mechanism supports the above methods to a certain extent, it could be a phenomenological understanding based on experience and sensitivity to displacement, material parameters, and compliance [116, 117]. In addition, the interval selection significantly affects the determination of the elastic–plastic transition force for the two-line and offset methods. Although the proposed methods ensure data repeatability, the accuracy of various methods still needs to be verified using CTT [118]. A series of modification methods [119] or new methods [120] have also been developed based on the above mainstream methods, such as the viewpoint of energy, which considers the energy before yield only related to the yield strength. Chen et al. [121, 122] proposed an analytical method based on the energy equivalence principle (EEP), which can accurately identify the yield strength of isotropic power-law materials. In addition to the existing identification of force–displacement and force–deflection curves, some innovative identification methods have been developed. Janča et al. [113] proposed a force–

Figure 4 Determination methods of elastic–plastic transition force [113].



thinning curve that subtracts deflection from displacement, which had certain advantages in plastic identification.

A series of database-based, inversion, and optimization methods have been proposed to study the anisotropy, strain rate sensitivity, stress state dependence, and damage-coupled constitutive, broadening the research field of vision [123, 124]. Algorithms such as enumeration, least squares-support vector machine, and gold section algorithm can inversely analyze the full-history stress–strain curve [125]. Calaf-Chica et al. [126] assumed 36 types of anisotropic materials, estimated the yield strength in combination with the Hill-48 yield criterion [119] and found that the SPT can provide a reference for evaluating the average value of six yield stress components. The residual deformation and the Bauschinger effect produced during manufacturing will cause the initial isotropic materials to become anisotropic, which could invalidate the existing yield strength prediction methods [127, 128]. The influences of the strain rate and stress state could also be considered in the SPT [129]. Test settings related to stress states are the directions for development, including the SDE of materials [116]. Cuesta et al. [90] proposed a dog bone SPT specimen to maintain a uniaxial stress state. Based on the study of stress state sensitivity. It can also explain that the difference in stress triaxiality (i.e., biaxial and uniaxial stress states) is the reason for the correlation deviation between SPT and CTT [130].

Failure parameter

In determining the failure parameters, multiple dependencies of the material type and direction should be considered [89], and an analytical method has yet to be widely accepted. The UTS is usually calculated using the maximum load point in the SPT, similar to the CTT. However, before reaching the maximum load, the specimen may have been thinned (corresponding to necking in the CTT) and fractured [92, 131], which can be observed by physical methods or identified by FEA [132]. Cuesta et al. [131] indicated that the maximum load was not the instant of initial crack propagation. The initial crack propagation point, which generally occurred at 70% of the maximum load, can be determined by observing the physical crack using the interrupted test method or measuring the flexibility mutation using the partial

unloading method. Altstadt et al. [92] confirmed that the material failed before reaching the maximum force, defined a force at the onset of plastic instability, and correlated it with UTS. The difference between the ball's displacement and deflection at the bottom of the specimen reflected the onset of plastic instability, and the difference from the maximum load point was approximately half.

The boundary conditions are described based on the notched specimen, temperature, stress state, and strain rate. Two methods could be used to determine fracture parameters. One is to find the correlation method based on the maximum deformation of the force–deflection curve; Another is to prefabricate various notches in specimens to trigger the stress concentration effect. The common notched SPT specimens are shown in Fig. 3. Under the same notch form, the location of the fracture is related to the friction coefficient and specimen thickness [117]. The restraint degree of the SPT notch specimen is still lower than that of the CTT notch specimen. SPT notch specimen may only apply to ductile materials because the loss of restraint may change the micro mechanism of fracture [98]. SPT notch specimens can also produce various stress states, such as the surface ring notch, which refers to the approximate plane strain state [100], and the through-thickness notch, which refers to the approximate plane stress state [99]. Meanwhile, some studies have focused on the sensitivity of temperature [133] and strain rate [110]. Pham et al. [109] discussed the effect of strain rate (deflection rate) on the deformation and fracture mechanisms. With an increase in loading speed, the time from void growth to final fracture was shortened, resulting in aggregation retardation; hence, the fracture toughness gradually decreased, and the fracture morphology changed [106].

Damage evolution and fracture strain are also the focus of this study. The multiaxial fracture strain energy density [134], ASME empirical formula [125], thickness change monitoring [114], DIC technology [135], and other methods can be used to obtain the fracture strain. After necking, the DIC measurement accuracy of SPT decreases compared with that of CTT but still maintains high repeatability [135]. Plastic instability occupies a large part of the SPT curve, and the stress triaxiality could be different from that of the CTT. Therefore, the microstructural evolution may differ, resulting in different deformation and fracture mechanisms. Damage coupling is considered

to characterize the macro deformation and failure behaviors [136]. The stress triaxiality and the Lode parameter describe the complete spatial stress state. Various notched specimens can provide a broader range of stress states and contribute to a complete damage model [137]. Most studies found that with an increase in the loading displacement, the fracture location gradually moved away from the center [138], with mesoscopic or phenomenological models such as the Gurson–Tvergaard–Needleman (GTN) [139] and modified Mohr–Coulomb [140] models. The actual stress state of the specimen is approximately a biaxial stress state with an inhomogeneous distribution [114]. The top surface is subjected to shear and compression stresses, and the bottom surface is subjected to tensile stress [125], which could lead to a different damage evolution mechanism, making it possible for non-single crack initiation [141]. The improvement of classical fracture criteria can consider more complex stress states, such as introducing a shear mechanism [142] and a brittle fracture mechanism [143]. In actual loading, the stress triaxiality gradually increases with the loading depth, and the average value is generally used (Table 3). Therefore, maintaining the stress triaxiality during the SPT to ensure the accuracy of the results should be attention when designing SPT specimens [144].

Data reliability of SPT

Size effect

The SPT specimen size is determined, and the range is narrow compared with specimens of STT and IT, resulting in less discussion on the size effect.

However, it must be addressed in SPT, especially for specimens composed of larger microstructures or unique processes. Cheng et al. [146] indicated that the shear mechanism was the main fracture factor in SPT, and the strain gradient plasticity based on the dislocation mechanism could be introduced to consider the size effect of smaller specimen size. Song et al. [147] manufactured specimens with different textures but similar grain sizes using different processes and found that SPT can capture the differences in mechanical properties caused by different specimen thicknesses, grain sizes, and thickness-to-grain size ratios. Wang et al. [148] conducted SPTs on specimens with different thicknesses and grain sizes and found that the material strength with coarse grain size increased with the decrease in thickness; the size dependence of the yield strength was stronger than that of the UTS, whereas the material strength value with fine grain size was independent of thickness. A theoretical model considering the density of GNDs, available dislocation source, and grain size was proposed to explain the different mechanical responses to specimen thicknesses, as shown in Fig. 5. The element sensitivity of FEA is also a manifestation of the size effect, which must be corrected to eliminate the influence [97] or avoided by non-local methods [149].

Inhomogeneity structure

As mentioned above, because the SPT specimen size does not descend to the micro- or nano-scale, the deviation caused by structural inhomogeneity is slight. The error of the structural inhomogeneity in the SPT is mainly caused by the thickness deviation

Table 3 Representative methods and formulas of SPT data correlation

Type	Parameters	Methods	Formulas	References
Elasticity	Young’s modulus	Initial slope method	$E = \lambda \cdot (k/h_0)$	[112]
Plasticity	Yield strength	Two-line series methods	$\sigma_y = \alpha_1 \cdot F_e/h_0^2 + \alpha_2$	[86–88]
		Energy method	$\sigma_y = \sqrt{\lambda E_{SP}}$	[145]
Failure	UTS	Maximum load method	$\sigma_u = \beta_1 \cdot F_m/h_0^2 + \beta_2$	[86–88]
		Load–displacement balance	$\sigma_u = \beta_1 \cdot F_m/(h_0 u_m) + \beta_2$	[111]
	Elongation	Proportional method	$A = \gamma_1 u_m + \gamma_2$	[133]
	Fracture strain	Thickness method	$\epsilon_f = \ln(h/h_f)$	[89]
Central deflection method		$\epsilon_f = \lambda(h/h_0)^\mu$	[117]	

where k is the slope in Stage I; E_{SP} is elastic energy; h_0 , h , and h_f are initial, instantaneous, and fracture thicknesses; u_m is the maximum deflection; F_m and F_e are the maximum and elastic–plastic transition forces; λ , μ , α_i , β_i , γ_i ($i = 1, 2$) are coefficients

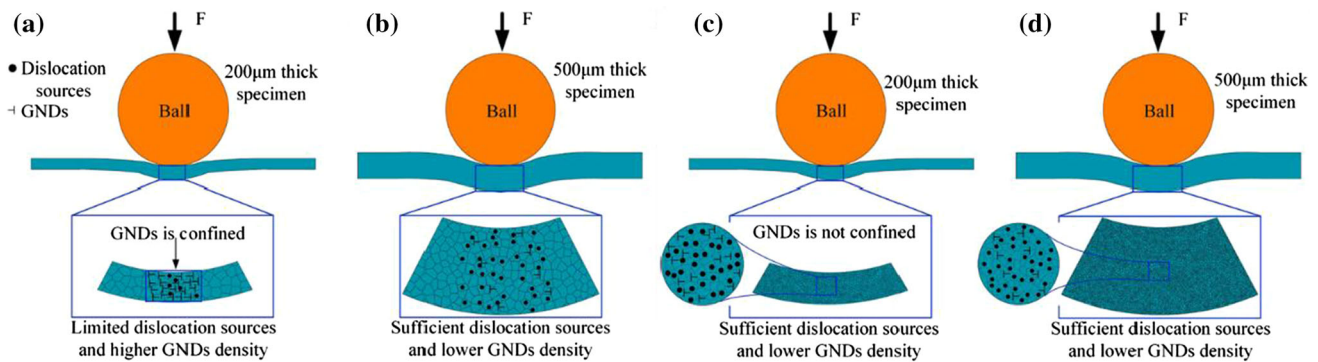


Figure 5 Dislocation sources and GNDs [148]. **a–b** Coarse grain size (50 μm). **c–d** Fine grain size (10 μm).

and inhomogeneous material. Altstadt et al. [150] systematically analyzed the repeatability and device dependence of the SPT results and confirmed the feasibility of identifying elastoplastic parameters. Guan et al. [151] studied the influence of inhomogeneous material characteristics of Q345R and Q235A, which were significant for the UTS but not for the yield strength. Yang et al. [152] studied the ultrasonic impact treatment of SS304 with a non-uniform surface and thickness and discussed the mechanical properties of materials with various grain sizes. Peng et al. [102] analyzed the sensitivity of the contact reaction to specimen parameters and found that a 5% deviation in thickness can cause significant changes in the SPT curve; the existing standard requires that the thickness deviation should not exceed 1% [86–88].

Manufacturing defect

This work mainly discusses the anisotropy caused by the preferred orientation of the microstructure or grains during manufacturing [127, 128], as well as the macro-anisotropy of materials caused by defects such as pores and inclusions, including elastoplastic and fracture anisotropy. Moreno-Valle et al. [153] studied the anisotropic deformation and fracture behaviors of coarse-grained commercially pure titanium after hydrostatic extrusion, which were related to the specific microstructure and texture. Rezaei et al. [154] conducted SPT on SLN IN718 and found that the comprehensive factors of sampling positions, specimen orientations, and residual stresses caused plastic anisotropy and different fracture mechanisms. Song et al. [155] studied the anisotropic fracture of A350 and found that the ordered distribution of pores and inclusions produced by manufacturing was the

reason for the anisotropic ductile or brittle fracture of SPT specimens.

Engineering application of SPT

SPTs are widely used to test the mechanical properties of irradiation equipment, pressure vessels, industrial components, WJs, and other devices and structures, which are non-uniform or deteriorate with time. Rodríguez et al. [156] considered the local porosity, sampling location, and sampling direction, and conducted SPT on the sintered product and welding HAZ to obtain the UTS of each zone. Rasche and Kuna [94] proposed that for a narrow weld of approximately 1 mm, the sampling slices could be parallel to the symmetry plane of the welded seam, and the result could correspond to the CTT of sampling perpendicular to the weld. Gülçimen et al. [157] carried out SPT on various zones of the P91 WJ and found that fine-grained HAZ had significant advantages in ductility and strength, while weld metal was temperature-sensitive and had relatively poor performance. Fan et al. [158] analyzed the significant effect of the inhomogeneous microstructure of SS316L multi-pass WJ on crack initiation and propagation and found that all zones of the WJ presented ductile fracture. The weld metal reduced the strength and ductility, and the HAZ exhibited high strength with low ductility, which was caused by the residual welding strain. Cuesta et al. [116] considered the influence of AA6061-T4 on the SPT under various pre-strains, providing a basis for testing the mechanical properties of stamping products at different positions. Gao et al. [159] studied the stress-strain characteristics of AA7075-T6 at various temperatures and strain rates and verified the thermo-plastic damage behavior combined with the GTN

model. Subsequently, the forming process of the automobile B-pillar was simulated, and it was found that the corner regions exhibited larger thinning than the flange region owing to the distribution of the void volume fraction.

Innovation of penetration test

The deviation of the punch geometry from a spherical shape will make the test no longer meet the definition of the SPT, but it is still a penetration test. These shape changes change not only the stress triaxiality but also the deformation and fracture mechanisms of the specimens [103]. For penetration tests, in addition to the common SPT, the small punch beam test [160] and SSPT [161] are similar to the SPT in the test device, loading mode, and response curve. Specimens of small punch beam test are composed of supported beams and cylindrical punches, which can ensure better machining accuracy compared with SPT. Zhuang et al. [162] considered the dimensional and shape error for the punch and proposed a flat punch with a semi-circular cross section and rectangular specimen. This small punch beam test configuration was insensitive to displacement rate and failure time, making it more suitable for measuring strain rate dependence. The SSPT is similar to fine blanking, and similar zones are distributed at the sheared edge: the rollover zone, shear zone, fracture zone, and burr zone. The rollover zone depends on plasticity; the shear zone presents a smooth fracture surface; the fracture zone produces an irregular and rough surface after crack onset; and the burr zone is caused by the final plastic deformation [161]. The research direction of SSPT is the same as that of SPT, such as device condition [163], specimen state [164], manufacturing process [165], and size effect [166]. Banafshi and Fereshteh-Saniee [161] proposed that the ratio of the die diameter to plate thickness should be within a specific range (2:1–10:1). Because a larger ratio increased the fracture zone, and a ratio that was too smaller increased the rollover zone, both exceeded will inhibit the formation of the shear zone, resulting in inaccurate shear strength measurement. Lancaster et al. [164] indicated a linear relationship between the data generated by SPT, SSPT, and CTT, and that SSPT was more advantageous in predicting UTS. Some researchers determined the correlation between various strengths and specimen parameters [166, 167] and found that the shear strength presented a size

effect when the thickness was below 200 μm [166]. The SSPT is especially suitable for materials with strain rate [168] or temperature [169] sensitivities and high ductility [170], which can produce large strain on small loading displacements because of the concentrated strain field. Zergani et al. [171] discussed the strain rate sensitivity and deformation mechanism of SS304L under various temperatures and found that the deformation mode was related to the gap and thickness; hence, a pure shear stress state could be maintained by adjusting the ratio. The SSPT is widely used to determine the local properties of stamped components [172] and WJs [173], which supports a large number of tests [174]. In addition, the general cylindrical punch can be changed to a rectangular section, which is suitable for identifying anisotropy [175].

Test of semi-penetration type

Configuration of IT

Background

The IT originates from the hardness–strength mapping based on hardness tests. The relevant test settings and definitions are inherited from the hardness test, including indenter shape and indentation depth classification. Commonly used indenters include flat-end cylindrical (also flat) indenters, sharp indenters, and rounded indenters. The flat-end cylindrical indenter provides a stable stress field, which is generally used for strain rate sensitivity. Both flat and sharp indenters produce a large range of plastic zone suitable for identifying fracture parameters, and the rounded indenter can measure the full-history elastoplastic behaviors [176]. The load and depth of indentation can be divided into macro-scale ($2 \text{ N} \leq F \leq 30 \text{ kN}$), micro-scale ($F < 2 \text{ N}$, $h > 200 \text{ nm}$), and nano-scale ($h \leq 200 \text{ nm}$) [176]. The data measured by various IT scales can realize the formula conversion of hardness–hardness or hardness–strength and form the corresponding standard [177]. Recently, an instrumented IT technique (generally nano-scale) with a specified indenter shape has been developed to automate the loading and displacement measurements of the indenter. The mainstream standards for instrumented IT include ISO 14577 [178], ASTM E2546 [179], GB/T 21838 [180], and GB/

T 22458 [181]. The ASTM standard only identifies hardness and modulus based on the Oliver–Pharr method. In contrast, the GB standard adds the continuous stiffness method (CSM) and indentation energy scale relationship (IESR) to the ASTM and ISO standards [181].

Geometry

Generally, sharp indenters include triangular pyramids, rectangular pyramids, and cone types; rounded indenters include spherical and cylindrical types; and flat indenters refer to column types. Several specific shapes are widely used, including triangular pyramid types containing Berkovich indenter, cube-corner indenter, rectangular pyramid types containing Vickers indenter, cone types containing Rockwell indenter, and spherical types containing Brinell (also sphere or ball) indenter. The classical indenters with specific characteristics are shown in Fig. 6. The four pyramidal surfaces of the Vickers indenter are difficult to intersect, resulting in the horizontal edge at the top and difficult-to-maintain self-similarity. Hence, a Berkovich indenter with the same projection area is designed. The cube-corner indenter is suitable for fracture toughness tests. The cone indenter is suitable for large-scale IT. The Brinell indenter, an irregular sphere (polyhedron) affected by the anisotropy of diamond, with small initial contact stress-producing only elastic deformation, is suitable for the elastoplastic test but not at the submicron-scale. IT with a flat indenter (also called impression test) presents a constant average contact stress under constant loading, resulting in a constant area of the plastic zone. Plastic deformation is related to the propagation of the plastic zone, which is suitable for the strain rate dependent test [182].

In order to simplify the analysis and directly establish a correlation relationship with the CTT curve, the characteristic strains of various indenter

shapes are defined to describe the indentation strain because of the complexity of the stress field beneath the indenter. Characteristic strain can be solved using the hardness and load definition methods [183]. The characteristic strain of self-similar indenters (such as cones or pyramids) is independent of indentation depth, whereas non-self-similar indenters (such as spheres) vary with indentation depth. With the development of indentation mechanism research, the theoretical model has gradually changed from a shear flow mechanism and an elastoplastic mechanism to a compression mechanism [176]. Factors affecting the IT response include device compliance, indenter shape, friction, residual stress, and strain hardening exponent. To reduce the effect of friction, the cone angle of pyramid indenters is generally designed to be large; cube-corner indenters with small equivalent cone angles present larger friction, which could change the contact mechanics mechanism [183]. Hardness is generally believed to be proportional to the yield stress when the specimen below the indenter is completely plastic.

Generally, the surface size of the specimen is not considered, and the thickness is selected as the maximum value between 2 mm and 20 times the indentation depth. As the indenter deepens, the material surrounding the indenter can be drawn inward or raised upward. Within the elastic limit, the material caves around the indenter, which is known as sink-in in most annealed materials, shown in Fig. 7a. As the deformation exceeds the elastic limit, the material is raised in the upward direction around the indenter, which is known as pile-up in most highly cold-worked materials, shown in Fig. 7b [176]. The existence of sink-in and pile-up phenomena would mislead the measurement of the indentation diameter, and the main influencing factors are the friction coefficient and hardening exponent. Ma et al. [184] proposed a method to identify the diameter of spherical indentation and found that the contact edge

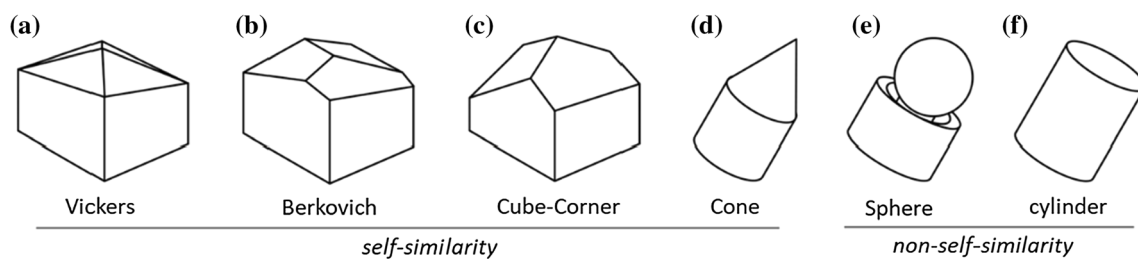


Figure 6 Geometries of indenters [24]. **a** Vickers. **b** Berkovich. **c** Cube-corner. **d** Cone. **e** Brinell. **f** Cylindrical.

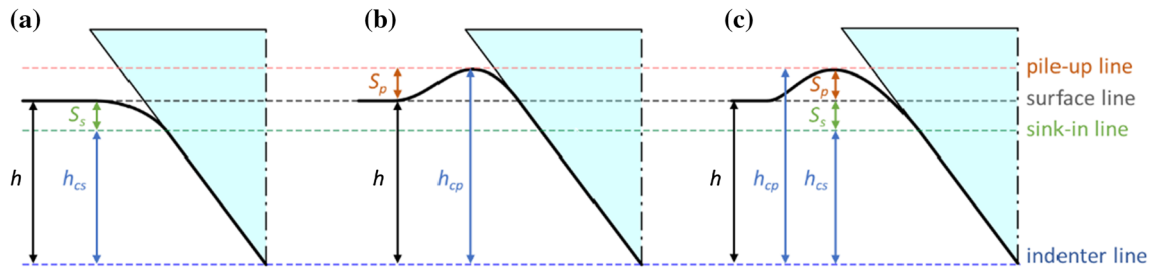


Figure 7 Indentation profiles [185]. **a** Sink-in phenomenon. **b** Pile-up phenomenon. **c** Coexistence phenomenon.

point occurred at the maximum slope angle change or the negative peak of the slope rate profile for both the loading and unloading conditions. The coexistence of sink-in and pile-up may occur for specific materials and loading conditions [185, 186], shown in Fig. 7c.

Test device

The processing quality of an indenter has a significant influence on the IT results. Most indenters can be seen as spherical crowns in a small size range; the smaller the radius of the indenter tip, the closer the actual indenter area function (IAF) is to the perfect IAF [183]. The triangular pyramid indenter is easier to grind with the highest processing quality, and the tip curvature of the Berkovich indenter is at least 20 nm; the rectangular pyramid inevitably exists as a transverse edge; the spherical indenter will present pyramid surfaces rather than an ideal sphere because of the anisotropy of the diamond crystal structure; the cylindrical indenter is fragile because of the hard and brittle characteristics of a diamond. The instabilities and errors measured by IT mainly include [183] the measurement equipment represented by indenter defects, contact zero, measuring resolution, electrical noise, and device compliance; the specimen surface quality represented by roughness, natural moisture absorption, work hardening during polishing, and residual stress; the material properties represented by sink-in and pile-up phenomena; the measurement environment represented by temperature, vibration, and noise; and the system parameter setting represented by indentation spacing and distance from the edge of the specimen. It is necessary to consider modified or new methods to improve the data reliability when the error is significant [187].

The stress–strain curve obtained from IT is usually processed using CSM, essentially the estimation of

the zero point and contact radius. The CSM errors include the following [188]: first, the load and displacement will be underestimated because the machine records the mean values during the oscillation cycle rather than the peak value; second, the contact stiffness will be underestimated because the ratio of the peak-to-peak amplitudes of the load and displacement signal is measured, whereas the actual load and displacement are nonlinear; and third, the loss of contact between the indenter tip and the specimen at low loads during the dynamic oscillations. Sudharshan Phani et al. [189] designed a device to maintain a constant indentation strain rate and developed a program to correct errors in the plastic stage, which improved the reliability of the CSM. Impact IT can also be established with a drop weight [190, 191], pendulum [192], and SHPB [193], and other aspects of the impact IT system also needs to be improved to avoid the influence of resonance, artifacts, and spring back in dynamic indentation [192, 194].

Data correlation of IT

Elastic parameter

The identification methods for Young's modulus include the single stiffness method (SSM) and CSM. The SSM is a quasi-static loading mode used to obtain the initial unloading stiffness with a loading–unloading process. The CSM superimposes a small dynamic alternating load based on SSM to produce a constant micro-amplitude displacement of the same frequency and measures the amplitude and phase difference of the alternating load and displacement signals to determine the change in contact stiffness with the indentation depth. The standards recommend three typical analysis methods for determining Young's modulus [178–181]. First, the contact stiffness and contact depth method (i.e., the Oliver–Pharr

method) is used to select the analysis parameters from the maximum load, IAF, and contact stiffness. The method presents a precise mechanical mechanism that is limited by the heavy dependence on IAF, which could underestimate the indentation area and overestimate the hardness and modulus when analyzing the pile-up or shallow indentation [183]. Second, the indentation energy and contact stiffness method, selecting the analysis parameters from the maximum load, contact stiffness, and the ratio of unloading work to total indentation work (UTIR), the IESR is established based on dimensional analysis. This method does not involve an IAF, which is suitable for sink-in and pile-up indentations but significantly influences the contact stiffness error. Third, the indentation energy method, which selects the analysis parameters from the ratio of the maximum load to the IAF and UTIR, the IESR is also established based on dimensional analysis. This method is also suitable for sink-in and pile-in indentations; however, the limitation lies in the difficulty of coefficient correction. The relationship between the analysis parameters and identification parameters limits their applicability [183]. For instance, the applicability of elastic contact theory in analyzing elastoplastic deformation with the Oliver–Pharr method, and the applicable scope and accuracy of the non-IESR with indentation energy analysis method [183].

The material properties can affect the degree of pile-up, and the work-hardening of the material surface around the indenter limits the material flow above the surface. Some indenter shapes, such as the Berkovich indenter, are insensitive to the pile-up phenomenon [195], but the indenter shapes affect the determination of Young's modulus. Liu et al. [196] indicated that the hardness of the Berkovich indenter was higher, and Young's modulus was lower than that of the cone indenter. Methods generally suitable for sink-in and pile-up phenomena have been widely studied. N'Jock et al. [197] proposed a method to calculate the elastoplastic parameters of a Vickers indenter by considering the ratio of the elastic recovery energy to the total indentation work rather than the contact area. Roa and Sirena [198] proposed a linear relationship between the ratio of elastic strain energy to total strain energy and the ratio of hardness to modulus with a cone indenter, which can effectively avoid the solution of IAF. Generally, a spherical indenter presents a long initial elastic stage, which is suitable for determining the elastic parameters. The

initial elastic stage of nano-IT only refers to a stroke of tens of nanometers; hence, the unloading method is commonly used to measure Young's modulus [188]. The data measured by micro or nano ITs could be necessary to verify the consistency and effectiveness of macro IT [199], and the measurement uncertainty under various scales should be considered [200]. Most methods currently rely on the known Poisson's ratio, whereas correlating elastic parameters directly from hardness has broader applicability [177]. Zorzi and Perottoni [201] discussed the empirical relationship between hardness and Young's modulus, which can accurately estimate Young's modulus and Poisson's ratio, thereby providing a reference for the performance measurement of new materials.

Plastic parameter

For the identification of plastic parameters, the Oliver–Pharr method based on the elastic contact theory has limitations determining yield, which could not be suitable for materials with apparent plastic plateaus. Several methods are provided to identify plastic parameters, such as the expanding cavity model (ECM), the representative strain method, and the self-similarity method. The ECM is a theoretical and analytical method; the self-similarity theory is used in the initial part of the plastic stage, and the slip-line theory is used in the latter part [183]. The representative strain method attempts to establish an equivalent relationship between the IT and CTT through massive tests [202]. The IT result refers to the coupling action between the indenter and the specimen. Hardness, a comprehensive mechanical parameter, makes the simple equivalent of a representative strain lack theorization [183]. Additional correction methods are still being explored [203]. Non-self-similarity (such as spherical) indenters are often used. For self-similarity indenters, the distribution of indentation stress and strain fields are self-similarities with the increase in indentation depth, which is not conducive to the decoupling of elasticity and plasticity [204]. For non-self-similarity indenters, the ratio of elastic deformation to plastic deformation changes during IT, which is conducive to decoupling and identification [182, 205].

The shape and size of the elastoplastic boundary must be partially captured in an idealized geometry. Hence, it is difficult to theoretically calculate the

contact stress of the elastoplastic indentation [206], which has led to the development of various numerical methods [207–209]. The method based on statistics is used to establish the correlation between indentation response and constitutive parameters according to massive FEA solutions and inverse the constitutive relationship from IT data (e.g., response surface and neural network methods) [210]. The methods are applicable for various situations, such as materials with apparent yield plateaus [211], identification with different indenter shapes [212], improvement of ECM to normalize formula [213] or speed up the calculation [214], parameter identification affecting different definitions of representative strain and contact radius [215], various stress states and strain states [216]. The energy method is insensitive to sink-in and pile-up phenomena [217], and the analytical formula has universality and a lower error than other empirical expressions [218]. Chen et al. [121, 219] proposed the total strain energy algorithm according to the integral mean value theorem (i.e., EEP), and it was successfully applied to the cone, spherical, cylindrical, and Vickers indenters [122]. The application condition of this principle is isotropic power-law material, which is universal for SPT and IT [122].

The strain rate effect is also an issue that can be easily ignored [135]. The Impact IT is usually carried out with a small drop weight rig [190]. It is difficult to dissipate heat at a high strain rate IT, presenting an adiabatic condition, which makes it difficult to identify the temperature sensitive constitutive relationship. Therefore, IT is often performed under low plastic strain to avoid excessive accumulation of plastic strain [190]. It is generally believed that the constraint factor obtained from quasi-static IT can be directly applied to dynamic IT and that the indentation strain rate is proportional to the equivalent uniaxial strain rate [183]. Ito and Arai [191] introduced a heat conduction equation into the ECM using the Johnson–Cook model to adapt to dynamic spherical indentation. Calle et al. [190] pointed out that the dilution of the high-strain-rate zone caused the non-uniform strain rate fields during spherical IT by the low strain rate of the large plastic zone as the indenter deepened, resulting in the strain rate traditionally defined to be larger than the actual situation. Saxena et al. [193] considered the influence of SDE on static and dynamic IT and found that the differences in the pile-up phenomenon and smoothness of the lip

were significantly different from the crater profiles of residual impressions. In addition, anisotropy is also a direction that is difficult to identify. Most existing studies rely on inverse identification methods such as optimization, neural networks, and machine learning [220], which depend on sink-in and pile-up phenomena [221]. Wang et al. [222] considered the potential uncertainty in optimization and identified plastic anisotropy based on Bayesian inference. Zhan et al. [223] modified the ECM with the Hill-48 model, considering the sink-in and pile-up phenomena, which can identify the out-of-plane anisotropy parameters of materials.

Failure parameter

For the identification of failure parameters, most studies have focused on the measurement of fracture toughness K_{IC} . Existing methods mainly include pyramidal (Vickers, Berkovich, cube-corner) indenters and spherical indenters. The crack length with a pyramid indenter can be accurately measured, but the elastic–plastic deformation field is challenging to analyze. The elastic deformation field with a spherical indenter is easy to analyze but lacks accuracy in measuring the crack length [183]. Even if the same indenter is used for IT, the indentation fracture morphology will differ owing to various factors [224], as shown in Fig. 8. The determination of the fracture toughness by IT is based on a certain approximation. In classical fracture mechanics, three necessary conditions are considered for testing K_{IC} [183]. First, the crack must be mode I, and the symmetry of IT can ensure that the crack is a mode I crack. Second, a plane strain state is required around the crack tip, which cannot be perfect around the radial crack tip; hence, the existing models generally introduce free surface influence factors for modification. Third, the analytical parameters are measured at the critical moment of crack propagation, while the actual crack size after unloading corresponds to the crack termination. During unloading, the radial crack continues to propagate under the action of the residual stress field, which is maintained before the crack stops. The third condition is approximately established when the parameter is similar to that at the end of the unloading. Lee et al. [224] found that ductile fracture was sensitive to Poisson's ratio because of the dependence of the indentation stress field on Poisson's ratio. Zhang et al. [225] discussed the

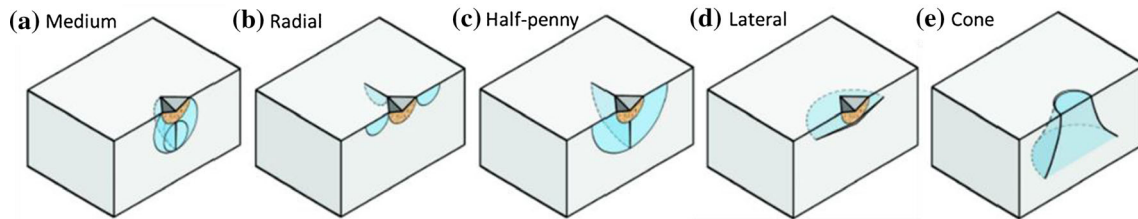


Figure 8 Representative crack morphologies in IT. **a** Medium crack. **b** Radial crack. **c** Half-penny crack. **d** Lateral crack. **e** Cone crack.

limitations of the Haggag toughness, critical indentation energy, critical stress–strain, and energy release rate models in identifying the fracture parameters of ductile metals. DIC is still a method for identifying plasticity, and it should be noted that DIC can only measure the strain field at the start and end moments of IT [226]. Strain field information can be identified by combining X-ray computed tomography with DVC [227].

It is expected that the device compliance will cause a reduction in the measured Young's modulus during loading, while few studies have focused on the degradation of Young's modulus due to the damage evolution, and their mechanisms are entirely different. The anisotropic damage caused by the shear and other mechanisms cannot be ignored during the loading process [228, 229]. Zou et al. [230] proposed a continuous indentation method to measure the area reduction rate to consider the damage evolution. The deformation was divided into two stages according to the change in modulus during unloading, and the critical point was regarded as the failure onset of materials below the indenter. For the study of damage failure, the GTN model based on micromechanics [231] and the continuum damage mechanics (CDM) model [232] are commonly used. Zhang et al. [229] proposed a shear-modified GTN model to describe the damage caused by indentation, considering the shear softening and localization owing to the nucleation of secondary and existing voids, which indicated the coexistence of shear softening and nucleation of secondary void mechanisms. Xue et al. [233] estimated the critical depth at the fracture instant by identifying the critical void volume fraction of the CDM model. Sun et al. [234] modified the ECM to accurately describe the stress triaxiality of a material under an indenter and found that the damage beneath the indenter was controlled by void nucleation induced by particle crushing. Ghosh et al. [235] conducted pre-strain IT based on the CDM model and found that the fracture toughness

decreased with an increase in pre-strain, which proved the strength deterioration of in-service materials. Wu et al. [236] normalized the dynamic strength and hardness and found that the thermal softening effect caused the loss of strain hardening ability under dynamic loading, which promoted the transformation to the shear failure mode, providing insights into the correlation between strength and hardness (Table 4). Future research could focus on the adaptability of the strain rate, stress state, anisotropy, SDE, and other aspects in the determination of fracture parameters [237].

Data reliability of IT

Size effect

A higher hardness at shallow indents can occur when intense forces are applied over a small area. During IT, the indented material underneath the indenter tip is deformed to generate dislocations, including GNDs and statistically stored dislocations (SSDs). While SSDs are randomly accumulated in the IT, GNDs are generated from the gradients of the plastic shear strain [238]. The density change of GNDs can describe the IT size effect, and the classical Nix–Gao model could adequately describe the indentation depth dependence of hardness in most metallic materials [239]. Various correction models were subsequently developed to avoid prediction deviation with a further reduction of indentation depth, such as SSDs and GNDs coupling [240] and elastic deformation effect [241]. At shallow indents, enormous stress is applied to induce plastic deformation, and numerous dislocations are created and stored in a slight deformation zone. These dislocations obstruct and interact with each other, leading to obstruction of dislocation motion. The obstructions are caused by the grain boundary, motions of dislocations, gliding of dislocations (easy slip systems) upon other non-easy slip systems, and other defects. In order to

Table 4 Representative methods and formulas of IT data correlation

Type	Parameters	Methods	Formulas	References
Elasticity	Young’s modulus	Standard method	$E = (1 - \nu_s^2) / [1/E_r - (1 - \nu_i^2)/E_i]$	[177–179]
Plasticity	Full-history	Load-indentation	$P_m = \lambda(d/d_i)^m$	[202]
		Flow stress-strain	$\sigma_{flow} = P_m/\psi, \epsilon^p = a/R$	[213]
		Representative strain	$\epsilon_r = \xi \tan \gamma$	[210]
		Modified ECM	$\sigma = \sqrt{[2E(W_e - U_i - U_e)] / [(2\pi/3)(3P/2\pi\sigma_e)^{3/2}]}$	[214]
Failure	UTS	EEP (Berkovich)	$\sigma_y = [(1 + n)(HB\pi D_B)^m] / [P^{m-1}\beta_1(e\beta_2/n)^n(1 + m)D_B^{2-m}]$	[121, 219]
		EEP (Vickers)	$\sigma_y = [HV(1 + n)] / [2\eta\beta_1(e\beta_2/n)^n \sin(\theta/2)]$	[121, 219]
	Damage	Load deviation	$D = (P_{m}^{ideal} - P_m) / P_{m}^{ideal}$	[234]

where E_r is reduced modulus; E_i is modulus of indenter; σ_{flow} is flow stress; σ_e is proportional limit; ϵ_r is representative strain; $\tan \gamma$ is shear strain at contact edges; ν_i and ν_s are Poisson’s ratios of indenter and specimen; P_m and P_m^{ideal} are mean and ideal loads; W_e is elastic part of external work; U_i and U_e are the elastic energies stored in indenter and specimen; D_B is the diameter of Berkovich indenter; θ is half-cone angle; R is radius of indenter tip; a is radius of the instantaneous contact boundary; d , and d_i are experimental, and indenter diagonals; m , n , ξ , and ψ are coefficients; e is natural constant; HV and HB are Vickers and Berkovich hardness

overcome these obstacles, stresses must increase continuously; thus, high stress (high hardness) and high density of dislocations are observed at shallow indentations [238]. The general IT identification methods are based on the isotropic Hertz contact theory. When the size effect is noticeable, the significant anisotropy (Young’s modulus and Poisson’s ratio) of grains must also be considered [188]. The pop-in shows that the indentation depth suddenly increases without an evident increase in the load, which is related to significant plastic deformation, resulting in the stress approaching the theoretical limit [188]. The pop-in is attributed to the size effect, and the indentation size at the yield point is equivalent to the dislocation network density (e.g., the dislocation spacing and cell size) [188]. The millisecond acquisition system usually cannot capture the actual material response, and the influence of the instrument on the measurement in the pop-in process is determined by inertia [242]. In addition, the indenter’s size effect should also be considered, especially the uniqueness of non-self-similar indenters. For spherical indenters, the consensus is that hardness is not affected by depth but increases with the decrease in the tip radius of the indenter [243]. Flat indenters have complex characteristics, affected by the coupling of the constant contact area and two length scales dependent pressure, singular plastic strain gradients at the sharp edges [244]. Yu et al. [245] proposed a closed-form expression of the cross-

scale indentation relationship based on the strain gradient plasticity theory and clarified the specific influences of indentation velocity, size effect, and initial porosity on the hardness and cavitation field in IT. Yin et al. [246] performed IT on gradient SS316L and found that the gradient layer thickness and grain size affected the strain rate sensitivity of the material, which presented an elastically homogenous but plastically gradient in nature. dos Santos et al. [247] studied the size effect induced by the plastic strain gradient in dynamic IT based on the porous plastic theory and found that the size effect hindered the emergence of plastic shock waves, which regularized the plastic shock wave and reduced the maximum plastic strain rate.

Inhomogeneity structure

Surface performance and flatness are essential factors to consider. Because IT is a surface probe technique, interference with the surface quality may affect the results. Considering the influence of surface modifications (e.g., coating, irradiation layer, and shot peening), an appropriate indenter should be selected because of the thin surface layer (approximately 1 μm); if the performance of the surface is not considered, it is necessary to remove the surface with a process does not produce an affected zone before IT [188]. The influence of surface quality can be summarized into three aspects [188]: a highly disturbed

surface layer produced by mechanical slicing and polishing methods, surface irregularities such as surface roughness or a thin oxide film on the surface, and the occurrence of pop-in at low loads. The rough specimen produces a significant error in IT. Marteau et al. [248] analyzed the sensitivity of parameters describing surface roughness and found that the root means square deviation had the greatest impact on hardness. Marimuthu et al. [249] proposed a two-stage flat-spherical indentation method for rough surfaces, suitable for non-uniform surfaces (roughness $R_a = 0\text{--}20\ \mu\text{m}$). In addition, the indentation spacing is also considered owing to the IT intensity, which is essentially the judgment of the minimum surface-affected zone. Sudharshan Phani and Oliver [250] evaluated the influence of Berkovich indentation spacing on the measured hardness and Young's modulus and found that a minimum indentation spacing of 10 times the indentation depth could be sufficient to obtain reliable results, which was less than half of the standard (20 times the indentation depth) [178–181].

Manufacturing defect

The difference in sharpness, which refers to manufacturing defects of the indenter or in-service wear, significantly impacts IT results, especially for shallow indentation depths. It could be explained as [183]: a sharp indenter presents an apparent boundary between the loading and unloading curve, indicating the material has undergone large plastic deformation; it can also find the large contact area of blunt indenter from the loading level, the contact area of blunt indenter will be much larger than the contact area of a sharp indenter under the same indentation depth, resulting in a considerable hardness. The elastic deformation of the indenter during loading also affects the IT results [251]. A certain inclination angle between the indenter and tested component generally exists owing to the device's tolerance and structure. Shahjahan and Hu [252] found that the influence of the angular deviation on IT can be ignored only when the deflection angle is less than 1.2° . In addition, various factors, such as the deformation behavior and mechanism affected by the grain orientation and boundary in the specimen [253], extra hardening caused by GNDS under the indenter [135], and the residual stress in tensile or compressive stress states [176], would affect the force level in IT.

Zhang et al. [254] analyzed the residual stress and plastic properties of specimens after uniaxial tension with spherical IT and found that the spherical characteristics of ECM were lost owing to the existence of residual stress, which needed to be further corrected, providing a reference for testing engineering components with residual stress and deformation.

Engineering application of IT

The indenter type can be flexibly selected for practical engineering applications. The Berkovich indenter is suitable for identifying hardness and Young's modulus; the Spherical indenter is considered to obtain a continuously varying indentation strain; the cylindrical indenter is used when a significant initial contact stiffness is expected [183]. Microstructural changes caused by heat treatment or stamping [255], engineering structures of welding or AM [256], and detection of large- or medium-sized in-service devices are all engineering testing scenarios of IT. Wu et al. [257] performed IT on austenitic SS304, identified the yield strength and UTS of local zones, and found a softening zone in the coarse-grained HAZ. Pham et al. [258] found that nano IT and micro IT are sensitive to metallurgical conditions during welding. Nano IT can obtain the mechanical properties of microstructural phases, and micro IT can obtain the mechanical properties of local zones to a certain extent. Peng et al. [66] carried out STT and micro IT on each zone of the Q345 WJ and proposed a method to obtain the hardening exponent from the microhardness based on Considère's necking criterion, which can accurately simulate the constitutive behavior in a large strain range. In addition, the temperature, strain rate, and stress state affecting materials' constitutive and failure behaviors are considered. Yonezu et al. [259] studied the mechanical properties of SS316L WJ at high temperatures and found that the local material properties improved due to welding thermal deformation. Awale et al. [260] conducted spherical IT on SS316LN and P91 dissimilar WJs and studied the mechanical properties related to the strain rate of each zone. Mohamadizadeh et al. [261] proposed a hardness correlation method to reasonably divide the WJ local zones of ultra-high-strength automotive steels, coupled the fracture strain measured by DIC to the meso-model of each zone, and simulated various failure modes of spot WJs. It should be noted that the two-dimensional

(plane stress state) fracture locus used in WJ local zones was approximated by the translation of the fracture locus of the base metal and then expanded to a three-dimensional fracture locus, which also provides a research direction for the spatialization of the fracture locus of the WJ.

Innovation of semi-penetration test

The IT still encounters opportunities and challenges, such as new plastic parameter identification methods and a more comprehensive range of specimen surface states. Campbell et al. [262] proposed a profilometry-based indentation plastometry method that can identify a full-history curve with good consistency with CTT. Sun et al. [263] developed a method for identifying Young's modulus of a microcapsule with a core-shell structure, expanding the identification object of IT. In fact, the current standards need to be more accurate to some extent. Zhang [183] believed that some definitions needed to be more accurate in ISO 14577 [178], such as "The mechanical work W_{total} indicated during the indentation procedure is only partly consumed as plastic deformation work W_{plast} . During the removal of the test force, the remaining part is set free as work of the elastic reverse deformation W_{elast} ". The area below the unloading curve was elastic work, and the energy unreleased during unloading was defined as plastic work, which confused the distinction between unloading work and elastic performance. However, during unloading, the elastic energy stored in the total indentation work was partially released in the unloading work mode, and the remainder was stored in the material under indentation, which is also the unloading difference between IT and CTT. After CTT unloading, only residual deformation existed, and the elastic energy was released entirely. After IT unloading, some elastic energy (approximately 40%) of the material beneath the indenter could not be released owing to residual indentation. This part of the elastic deformation energy and plastic dissipation energy should be differentially treated because they can be released under specific conditions. The relevant definitions and descriptions have been modified [183] in GB/T 22458 [181]. Generally, it is a misunderstanding of the mechanical concept that does not affect the solution of mechanical properties in previous studies. However, the definition of relevant parameters in

standards should be considered more cautiously, and a cooperative agreement should be reached.

Summary and outlook

In this work, a series of SSTT tests were classified according to specimen geometry and loading features; that is, a similarity test with a geometry and loading method similar to CTT, a penetration test with a thin specimen punched through, a semi-penetration test with a specimen indented. The progressiveness and limitations of each type of typical test (i.e., STT, SPT, IT) were reviewed. (a) The STT is convenient for sampling, and the loading process is consistent with the CTT under the premise that the specimen geometry is similar, resulting in satisfactory analysis complexity, device compatibility, and testing repetition numbers. (b) The SPT specimen is in an approximate biaxial stress state during loading, which refers to the compression-shear state of the contact surface and tension state of the opposite side, resulting in less sampling, data stability, and broad applicability. (c) The IT is a non-destructive test, which refers to the compression state of the contact surface and no deformation of the opposite side, resulting in non-preparation required, massive test ability, and test portability; however, surface quality and data scattering should be considered. These three types of tests may have some differences in specimen geometries, test devices, loading methods, or data processing, but are all faced with data reliability issues of size effects, inhomogeneity structures, and manufacturing defects.

Many commonalities are reflected not only between similarity tests and conventional tests but also between penetration tests and semi-penetration tests. Penetration and semi-penetration tests are the intrusions of external elastoplastic or rigid loading bodies into specimens with a consistent loading mode. The stress and strain states on the contact surface are the same, and the solution methods of deformation and failure parameters also have some similarities (such as continuous unloading to solve Young's modulus). The loading bodies of the SPT and spherical IT are both spherical shapes, and the loading bodies of the SPT and cylindrical IT are both flat shapes. Conical and pyramid-shaped loading bodies may also be applied to penetration tests to introduce the progressiveness of self-similarity and

anisotropic adaptability in semi-penetration tests into penetration tests.

Different types of tests have different scopes of applications. In the study of fractures, similarity types and penetration types can quickly identify the fracture strain, whereas the semi-penetration type should establish a theoretical assumption model with a particular difficulty [234]. The advantage of a similar type is obvious when it comes to the stress state sensitivity of fracture. The stress states of specimens in similarity tests and conventional tests are consistent, such as the uniaxial stress state in STT and CTT, and the penetration test represented by SPT is in a biaxial stress state. In order to adapt to a broader range of stress states, SPT specimens need to be improved and innovated [101]. When SDE is involved, only the STT is suitable because of the test features. Current studies on notched SPT specimens have mainly focused on fracture toughness rather than fracture strain [99]. All types of tests are performed for temperature and strain rate sensitivity tests. However, it should be noted that the deformation behaviors of the specimens are different; hence, methods to maintain the constant strain rate deformation of specimens could also be different [264].

SSTTs can still be developed considerably, especially when testing the deformation and failure properties of metallic materials [183]. This development can include expanding similarity, penetration, and semi-penetration test methods; cross-referencing the advantages of specimen designs and test devices; accurately defining various tests with broad consensus; improving specimens for stress state sensitivity; improving the robustness of various tests under medium and high strain rates; broadening the applicability of parameter solving methods under specific studies; correcting data reliability such as size effects; further researching the problem of data scattering. By focusing on these directions, SSTTs will be used as alternative tests instead of complementary tests.

Acknowledgements

This work was supported by the National Natural Science Foundation of China (52175123), Outstanding Youth Science and Technology Talents Program of Sichuan (2022JDJQ0025), and International Science

and Technology Innovation Cooperation Project of Sichuan Province (2022YFH0075).

References

- [1] Karthik V, Kasiviswanathan KV, Raj B (2016) Miniaturized testing of engineering materials. CRC Press, Boca Raton
- [2] Kumar K, Madhusoodanan K, Singh RN (2017) Miniature test techniques for life management of operating equipment. *Nucl Eng Des* 323:345–358. <https://doi.org/10.1016/j.nucengdes.2017.03.007>
- [3] Kashaev N, Horstmann M, Ventzke V, Riekehr S, Huber N (2013) Comparative study of mechanical properties using standard and micro-specimens of base materials Inconel 625, Inconel 718 and Ti–6Al–4V. *J Mater Res Technol-JMRT* 2:43–47. <https://doi.org/10.1016/j.jmrt.2013.03.003>
- [4] Hwang J-K (2019) Effects of diameter and preparation of round shaped tensile specimen on mechanical properties. *Mater Sci Eng A-Struct* 763:138119. <https://doi.org/10.1016/j.msea.2019.138119>
- [5] Molak RM, Kartal ME, Pakiela Z, Kurzydowski KJ (2016) The effect of specimen size and surface conditions on the local mechanical properties of 14MoV6 ferritic–pearlitic steel. *Mater Sci Eng A-Struct* 651:810–821. <https://doi.org/10.1016/j.msea.2015.11.037>
- [6] Courtright ZS, Leclerc NP, Kim HN, Kalidindi SR (2021) Critical comparison of spherical microindentation, small punch test, and uniaxial tensile testing for selective laser melted Inconel 718. *Appl Sci-Basel* 11:1061. <https://doi.org/10.3390/app11031061>
- [7] ISO 6892-1 (2019) Metallic materials—Tensile testing—Part 1: Method of test at room temperature
- [8] ASTM E8/E8M-21 Standard test methods of tension testing of metallic materials
- [9] GB/T 228.1-2021 Metallic materials—Tensile testing—Part 1: method of test at room temperature
- [10] Gussev MN, Howard RH, Terrani KA, Field KG (2017) Sub-size tensile specimen design for in-reactor irradiation and post-irradiation testing. *Nucl Eng Des* 320:298–308. <https://doi.org/10.1016/j.nucengdes.2017.06.008>
- [11] Džugan J, Konopik P, Rund M, Prochazka R (2015) Determination of local tensile and fatigue properties with the use of sub-sized specimens. In: ASME 2015 pressure vessels and piping conference, Vol 1A, Codes and Standards
- [12] Dymáček P, Jarý M, Dobeš F, Kloc L (2018) Tensile and creep testing of Sanicro 25 using miniature specimens. *Materials* 11:142. <https://doi.org/10.3390/ma11010142>

- [13] Zhang Z, Liu X, Zheng P, Chen J, Cai L, Chen H, Che T (2021) A small specimen testing method to determine tensile properties of metallic materials. *Fusion Eng Des* 164:112148. <https://doi.org/10.1016/j.fusengdes.2020.112148>
- [14] Zheng P, Chen R, Liu H, Chen J, Zhang Z, Liu X, Shen Y (2020) On the standards and practices for miniaturized tensile test—a review. *Fusion Eng Des* 161:112006. <https://doi.org/10.1016/j.fusengdes.2020.112006>
- [15] Zhang L, Harrison W, Yar MA, Brown SG, Lavery NP (2021) The development of miniature tensile specimens with non-standard aspect and slimmness ratios for rapid alloy prototyping processes. *J Mater Res Technol-JMRT* 15:1830–1843. <https://doi.org/10.1016/j.jmrt.2021.09.029>
- [16] Cruz DJ, Shamchi SP, Santos AD, Amaral RL, Tavares PJ, Moreira P (2020) Development of a mini-tensile approach for sheet metal testing using Digital Image Correlation. *Procedia Struct Integr* 25:316–323. <https://doi.org/10.1016/j.prostr.2020.04.036>
- [17] Liu H, Chen R, Wen M, Zhang L, Shen Y (2019) Optimizing parallel section length for small tensile specimen with fabrication non-uniformity in thickness. *Fusion Eng Des* 147:111244. <https://doi.org/10.1016/j.fusengdes.2019.111244>
- [18] Yuan WJ, Zhou F, Zhang ZL, Su YJ, Qiao LJ, Chu WY (2013) An analysis on necking effect and stress distribution in round cross-section specimens of pure copper with different diameters. *Mater Sci Eng A-Struct* 561:183–190. <https://doi.org/10.1016/j.msea.2012.10.077>
- [19] Yuan WJ, Zhang ZL, Su YJ, Qiao LJ, Chu WY (2012) Influence of specimen thickness with rectangular cross-section on the tensile properties of structural steels. *Mater Sci Eng A-Struct* 532:601–605. <https://doi.org/10.1016/j.msea.2011.11.021>
- [20] Bergonzi L, Vettori M, Pirondi A (2019) Development of a miniaturized specimen to perform uniaxial tensile tests on high performance materials. *Procedia Struct Integr* 24:213–224. <https://doi.org/10.1016/j.prostr.2020.02.018>
- [21] Balakrishnan KS, Samal MK, Parashar J, Tiwari GP, Anatharaman S (2014) Suitability of miniature tensile specimens for estimating the mechanical property data of pressure tubes: an assessment. *Trans Indian Inst Met* 67:47–55. <https://doi.org/10.1007/s12666-013-0316-0>
- [22] Howard C, Judge CD, Hosemann P (2019) Applying a new push-to-pull micro-tensile testing technique to evaluate the mechanical properties of high dose Inconel X-750. *Mater Sci Eng A-Struct* 748:396–406. <https://doi.org/10.1016/j.msea.2019.01.113>
- [23] Lucon E (2014) Testing of small-sized specimens. In: *Comprehensive materials processing*. Elsevier, pp 135–163
- [24] Liu H (2020) A study on ultra-small specimen mechanical test methods: specimen geometry optimization, data conversion method and feasibility analysis, China
- [25] Kazakeviciute J, Rouse JP, Focatiis D, Hyde C (2022) Small specimen techniques for estimation of tensile, fatigue, fracture and crack propagation material model parameters. *J Strain Anal Eng Des* 57:227–254. <https://doi.org/10.1177/030932472111025208>
- [26] Kahl S, Peng RL, Calmunger M, Olsson B, Johansson S (2014) In situ EBSD during tensile test of aluminum AA3003 sheet. *Micron* 58:15–24. <https://doi.org/10.1016/j.micron.2013.11.001>
- [27] Nozawa T, Sakasegawa H, Chen X, Kato T, Geringer JW, Katoh Y, Tanigawa H (2020) Non-contact strain evaluation for miniature tensile specimens of neutron-irradiated F82H by digital image correlation. *Fusion Eng Des* 157:111663. <https://doi.org/10.1016/j.fusengdes.2020.111663>
- [28] Kato T, Ohata M, Nogami S, Tanigawa H (2016) Evaluation of impacts of stress triaxiality on plastic deformability of RAFM steel using various types of tensile specimen. *Fusion Eng Des* 109–111:1631–1636. <https://doi.org/10.1016/j.fusengdes.2015.11.003>
- [29] Ma ZC, Zhao HW, Wang KT, Zhou XQ, Hu XL, Lu S, Cheng HB (2013) Note: investigation on the influences of gripping methods on elastic modulus by a miniature tensile device and in situ verification. *Rev Sci Instrum* 84:66102. <https://doi.org/10.1063/1.4808374>
- [30] Venkatachalam S, Banjare R, Murthy H, Rao BC (2019) Mechanical testing of micro-specimens of Al6061-T6 using DIC for strain measurement. *Exp Tech* 43:125–135. <https://doi.org/10.1007/s40799-018-0254-1>
- [31] Ma Z, Zhao H, Wang K, Zhou X, Hu X, Lu S, Cheng H (2013) Novel correction methods on a miniature tensile device based on a modular non-standard layout. *Meas Sci Technol* 24:85901. <https://doi.org/10.1088/0957-0233/24/8/085901>
- [32] Hajy Akbary F, Santofimia MJ, Sietsma J (2014) Elastic strain measurement of miniature tensile specimens. *Exp Mech* 54:165–173. <https://doi.org/10.1007/s11340-013-9785-7>
- [33] Yang B, Sun W-Q, Jiang W-C, Wang M-L, Li M-C, Chen J-K (2019) Comparative study of the tensile properties of a 1.25Cr-0.5Mo steel characterized by the miniature specimen and the standard specimen. *Int J Pressure Vessel Pip* 177:103990. <https://doi.org/10.1016/j.ijpvp.2019.103990>
- [34] Merezhko MS, Merezhko DA, Rofman OV, Dikov AS, Maksimkin OP, Short MP (2022) Macro-Scale strain localization in highly irradiated stainless steel investigated using digital image correlation. *Acta Mater* 231:117858. <https://doi.org/10.1016/j.actamat.2022.117858>

- [35] McClintock DA, Gussev MN, Campbell C, Mao K, Lach TG, Lu W, Hachtel JA, Unocic KA (2022) Observations of radiation-enhanced ductility in irradiated Inconel 718: Tensile properties, deformation behavior, and microstructure. *Acta Mater* 231:117889. <https://doi.org/10.1016/j.actamat.2022.117889>
- [36] Gussev MN, Byun TS, Busby JT (2012) Description of strain hardening behavior in neutron-irradiated FCC metals. *J Nucl Mater* 427:62–68. <https://doi.org/10.1016/j.jnucmat.2012.04.017>
- [37] Kamaya M, Kitsunai Y, Koshiishi M (2015) True stress–strain curve acquisition for irradiated stainless steel including the range exceeding necking strain. *J Nucl Mater* 465:316–325. <https://doi.org/10.1016/j.jnucmat.2015.05.027>
- [38] McClintock DA, Gussev MN, Campbell C, Lu W (2021) Characterization of mechanical properties and deformation behavior of highly irradiated 316L stainless steel from target modules at the Spallation Neutron Source using digital image correlation analysis. *J Nucl Mater* 545:152729. <https://doi.org/10.1016/j.jnucmat.2020.152729>
- [39] Rund M, Procházka R, Konopík P, Džugan J, Folgar H (2015) Investigation of sample-size influence on tensile test results at different strain rates. *Procedia Eng* 114:410–415. <https://doi.org/10.1016/j.proeng.2015.08.086>
- [40] Anderson D, Winkler S, Bardelcik A, Worswick MJ (2014) Influence of stress triaxiality and strain rate on the failure behavior of a dual-phase DP780 steel. *Mater Des* 60:198–207. <https://doi.org/10.1016/j.matdes.2014.03.073>
- [41] Zhang Y, Karnati S, Pan T, Liou F (2020) Determination of constitutive relation from miniature tensile test with digital image correlation. *J Strain Anal Eng Des* 55:99–108. <https://doi.org/10.1177/0309324719892732>
- [42] Kumar K, Pooleery A, Madhusoodanan K, Singh RN, Chatterjee A, Dutta BK, Sinha RK (2016) Optimisation of thickness of miniature tensile specimens for evaluation of mechanical properties. *Mater Sci Eng A Struct* 675:32–43. <https://doi.org/10.1016/j.msea.2016.08.032>
- [43] Lall A, Bowen P, Rabiei A (2022) A numerical and experimental approach to compare the effect of sample thickness in small in-situ SEM and large ex-situ tensile testing in Alloy 709. *Mater Charact* 184:111614. <https://doi.org/10.1016/j.matchar.2021.111614>
- [44] Yang B, Xuan F-Z, Chen J-K (2018) Evaluation of the microstructure related strength of CrMoV weldment by using the in-situ tensile test of miniature specimen. *Mater Sci Eng A Struct* 736:193–201. <https://doi.org/10.1016/j.msea.2018.08.099>
- [45] Sun X, Soulami A, Choi KS, Guzman O, Chen W (2012) Effects of sample geometry and loading rate on tensile ductility of TRIP800 steel. *Mater Sci Eng A Struct* 541:1–7. <https://doi.org/10.1016/j.msea.2011.12.115>
- [46] Arnaud P, Heripre E, Douit F, Aubin V, Fouvry S, Guiheux R, Branger V, Michel G (2021) Micromechanical tensile test investigation to identify elastic and toughness properties of thin nitride compound layers. *Surf Coat Technol* 421:127303. <https://doi.org/10.1016/j.surfcoat.2021.127303>
- [47] Xing L, Zhan M, Gao PF, Li M, Dong YD, He WW (2020) The interactive effect of microstructure and stress state on the microscopic damage development of aluminum alloy tailor-welded blank. *Mater Des* 193:108836. <https://doi.org/10.1016/j.matdes.2020.108836>
- [48] Azghandi SM, Weiss M, Arhatari BD, Adrien J, Maire E, Barnett MR (2020) A rationale for the influence of grain size on failure of magnesium alloy AZ31: An in situ X-ray microtomography study. *Acta Mater* 200:619–631. <https://doi.org/10.1016/j.actamat.2020.09.016>
- [49] Hou Y, Zhang W, Mi X, Xie H, Feng X, Huang G, Peng L, Yang Z (2022) Different response mechanisms of yield strength and ultimate tensile strength in pure copper considering size effect. *Mater Sci Eng A Struct* 849:143443. <https://doi.org/10.1016/j.msea.2022.143443>
- [50] Wharry JP, Yano KH, Patki PV (2019) Intrinsic-extrinsic size effect relationship for micromechanical tests. *Scr Mater* 162:63–67. <https://doi.org/10.1016/j.scriptamat.2018.10.045>
- [51] Chen F, Chen S, Dong XH, Li CY, Hong XT, Zhang XP (2015) Size effects on tensile strength of aluminum–bronze alloy at room temperature. *Mater Des* 85:778–784. <https://doi.org/10.1016/j.matdes.2015.06.169>
- [52] Yalçinkaya T, Özdemir İ, Simonovski I (2018) Micromechanical modeling of intrinsic and specimen size effects in microforming. *Int J Mater Form* 11:729–741. <https://doi.org/10.1007/s12289-017-1390-3>
- [53] Zhu C, Xu J, Yu H, Shan D, Guo B (2021) Size effect on the high strain rate micro/meso-tensile behaviors of pure titanium foil. *J Mater Res Technol-JMRT* 11:2146–2159. <https://doi.org/10.1016/j.jmrt.2021.02.022>
- [54] Ando M, Tanigawa H, Kurotaki H, Katoh Y (2018) Mechanical properties of neutron irradiated F82H using micro-tensile testing. *Nucl Mater Energy* 16:258–262. <https://doi.org/10.1016/j.nme.2018.07.008>
- [55] Xu A, Yang C, Thorogood G, Bhattacharyya D (2020) Investigating bulk mechanical properties on a micro-scale: micro-tensile testing of ultrafine grained Ni–SiC composite to determine its fracture mechanism and strain rate

- sensitivity. *J Alloy Compd* 817:152774. <https://doi.org/10.1016/j.jallcom.2019.152774>
- [56] Dehm G, Jaya BN, Raghavan R, Kirchlechner C (2018) Overview on micro- and nanomechanical testing: new insights in interface plasticity and fracture at small length scales. *Acta Mater* 142:248–282. <https://doi.org/10.1016/j.actamat.2017.06.019>
- [57] Dzugan J, Seifi M, Prochazka R, Rund M, Podany P, Konopik P, Lewandowski JJ (2018) Effects of thickness and orientation on the small scale fracture behaviour of additively manufactured Ti–6Al–4V. *Mater Charact* 143:94–109. <https://doi.org/10.1016/j.matchar.2018.04.003>
- [58] Kumar K, Pooleery A, Madhusoodanan K, Singh RN, Chakravarty JK, Dutta BK, Sinha RK (2014) Use of miniature tensile specimen for measurement of mechanical properties. *Procedia Eng* 86:899–909. <https://doi.org/10.1016/j.proeng.2014.11.112>
- [59] Kale AB, Singh J, Kim B-K, Kim D-I, Choi S-H (2020) Effect of initial microstructure on the deformation heterogeneities of 316L stainless steels fabricated by selective laser melting processing. *J Mater Res Technol-JMRT* 9:8867–8883. <https://doi.org/10.1016/j.jmrt.2020.06.015>
- [60] Fang M, Li Y, Han Y, Le J, Huang G, Chai X, Lei L, Lu W (2022) In-situ investigation on the anisotropic behavior of the additively manufactured dual-phase Ti–6Al–4V alloy. *Mater Charact* 189:112003. <https://doi.org/10.1016/j.matchar.2022.112003>
- [61] Benzing JT, Liew LA, Hrabe N, DelRio FW (2020) Tracking defects and microstructural heterogeneities in meso-scale tensile specimens excised from additively manufactured parts. *Exp Mech* 60:165–170. <https://doi.org/10.1007/s11340-019-00558-4>
- [62] Ma Y, Takikawa A, Nakanishi J, Doira K, Shimizu T, Lu Y, Ma N (2021) Measurement of local material properties and failure analysis of resistance spot welds of advanced high-strength steel sheets. *Mater Des* 201:109505. <https://doi.org/10.1016/j.matdes.2021.109505>
- [63] Sridharan N, Gussev M, Seibert R, Parish C, Norfolk M, Terrani K, Babu SS (2016) Rationalization of anisotropic mechanical properties of Al-6061 fabricated using ultrasonic additive manufacturing. *Acta Mater* 117:228–237. <https://doi.org/10.1016/j.actamat.2016.06.048>
- [64] Luo C, Zhang Y (2019) Constitutive relationship of fusion zone in the spot welds of advance high strength steels. *J Manuf Process* 45:624–633. <https://doi.org/10.1016/j.jmpro.2019.08.007>
- [65] Manikandan P, Prabhu TA, Manwatkar SK, Rao GS, Murty SVSN, Sivakumar D, Pant B, Mohan M (2021) Tensile and fracture properties of aluminium alloy AA2219-T87 friction stir weld joints for aerospace applications. *Metall Mater Trans A* 52:3759–3776. <https://doi.org/10.1007/s11661-021-06337-y>
- [66] Peng Y, Wu C, Gan J, Dong J (2019) Characterization of heterogeneous constitutive relationship of the welded joint based on the stress-hardness relationship using micro-hardness tests. *Constr Build Mater* 202:37–45. <https://doi.org/10.1016/j.conbuildmat.2018.12.218>
- [67] Peng Y, Wu C, Gan J, Dong J (2018) Determination of the local constitutive properties of the welded steel joints using digital image correlation method. *Constr Build Mater* 171:485–492. <https://doi.org/10.1016/j.conbuildmat.2018.03.182>
- [68] Ambriz RR, Froustey C, Mesmacque G (2013) Determination of the tensile behavior at middle strain rate of AA6061-T6 aluminum alloy welds. *Int J Impact Eng* 60:107–119. <https://doi.org/10.1016/j.ijimpeng.2013.04.006>
- [69] Suthar H, Bhattacharya A, Paul SK (2020) Local deformation response and failure behavior of AA6061-AA6061 and AA6061-AA7075 friction stir welds. *CIRP J Manuf Sci Technol* 30:12–24. <https://doi.org/10.1016/j.cirpj.2020.03.006>
- [70] Suthar H, Bhattacharya A, Paul SK (2021) Determination of local constitutive properties in similar and dissimilar friction stir welded joints from DIC based surface strain measurement in two mutually perpendicular surfaces. *Mech Mater* 160:103930. <https://doi.org/10.1016/j.mechmat.2021.103930>
- [71] Suthar H, Bhattacharya A, Paul SK (2022) DIC-based approach to predict post necking behavior for AA6061, AA7075 and their friction stir welded joints. *Mech Mater* 172:104364. <https://doi.org/10.1016/j.mechmat.2022.104364>
- [72] Yan R, El Bamby H, Veljkovic M, Xin H, Yang F (2021) A method for identifying the boundary of regions in welded coupon specimens using digital image correlation. *Mater Des* 210:110073. <https://doi.org/10.1016/j.matdes.2021.110073>
- [73] Hosemann P (2018) Small-scale mechanical testing on nuclear materials: bridging the experimental length-scale gap. *Ser Mater* 143:161–168. <https://doi.org/10.1016/j.scripamat.2017.04.026>
- [74] Bakaev A, Terentyev D, Zinovev A, Chang C-C, Yin C, Bakaev VA, Zhurkin EE (2022) Application of sub-miniaturized bending tests to extract tensile properties from neutron-irradiated metallic alloys. *J Nucl Mater* 558:153320. <https://doi.org/10.1016/j.jnucmat.2021.153320>
- [75] Rajpoot D, Tandaiya P, Narayan RL, Ramamurty U (2022) Size effects and failure regimes in notched micro-cantilever

- beam fracture. *Acta Mater* 234:118041. <https://doi.org/10.1016/j.actamat.2022.118041>
- [76] Kazakeviciute J, Rouse JP, de Focatiis D, Hyde CJ (2019) The development of a novel technique for small ring specimen tensile testing. *Theor Appl Fract Mech* 99:131–139. <https://doi.org/10.1016/j.tafmec.2018.11.016>
- [77] Chen H, Cai LX (2017) Unified ring-compression model for determining tensile properties of tubular materials. *Mater Today Commun* 13:210–220. <https://doi.org/10.1016/j.mtcomm.2017.10.006>
- [78] Chatterjee A, Kumar K, Gopalan A, Devi YP, Singh RN, Sinha SK (2022) Miniature impact test technique to evaluate the orientation dependence of impact toughness of hydrided Zr–2.5%Nb alloy. *Int J Fract* 233:195–210. <https://doi.org/10.1007/s10704-022-00619-1>
- [79] Reichardt A, Lupinacci A, Frazer D, Bailey N, Vo H, Howard C, Jiao Z, Minor AM, Chou P, Hosemann P (2017) Nanoindentation and in situ microcompression in different dose regimes of proton beam irradiated 304 SS. *J Nucl Mater* 486:323–331. <https://doi.org/10.1016/j.jnucmat.2017.01.036>
- [80] Rovaris F, Papanikolaou S, Alava MJ (2022) Effects of surface curvature and dislocation dynamics: dynamical deformation mechanisms for uniaxial compression tests at the nanoscale. *Mater Sci Eng A-Struct* 846:143270. <https://doi.org/10.1016/j.msea.2022.143270>
- [81] Jedrasiak P, Shercliff H (2021) Finite element analysis of small-scale hot compression testing. *J Mater Sci Technol* 76:174–188. <https://doi.org/10.1016/j.jmst.2020.11.007>
- [82] Kitamura K, Terano M (2014) Determination of local properties of plastic anisotropy in thick plate by small-cube compression test for precise simulation of plate forging. *CIRP Ann-Manuf Technol* 63:293–296. <https://doi.org/10.1016/j.cirp.2014.03.038>
- [83] Mueller MG, Fornabaio M, Žagar G, Mortensen A (2016) Microscopic strength of silicon particles in an aluminium–silicon alloy. *Acta Mater* 105:165–175. <https://doi.org/10.1016/j.actamat.2015.12.006>
- [84] Armstrong D, Hardie CD, Gibson J, Bushby AJ, Edmondson PD, Roberts SG (2015) Small-scale characterisation of irradiated nuclear materials: part II nanoindentation and micro-cantilever testing of ion irradiated nuclear materials. *J Nucl Mater* 462:374–381. <https://doi.org/10.1016/j.jnucmat.2015.01.053>
- [85] Ast J, Ghidelli M, Durst K, Göken M, Sebastiani M, Korsunsky AM (2019) A review of experimental approaches to fracture toughness evaluation at the micro-scale. *Mater Des* 173:107762. <https://doi.org/10.1016/j.matdes.2019.107762>
- [86] ASTM E3205-20 Standard test method for small punch testing of metallic materials
- [87] EN 10371:202 1Metallic materials—Small punch test method
- [88] GB/T 29459.2-2012 Small punch test methods of metallic materials for in-service pressure equipments—part 2: method of test for tensile properties at room temperature
- [89] Torres J, Gordon AP (2021) Mechanics of the small punch test: a review and qualification of additive manufacturing materials. *J Mater Sci* 56:10707–10744. <https://doi.org/10.1007/s10853-021-05929-8>
- [90] Cuesta II, Rodríguez C, García TE, Alegre JM (2015) Effect of confinement level on mechanical behaviour using the small punch test. *Eng Fail Anal* 58:206–211. <https://doi.org/10.1016/j.engfailanal.2015.09.008>
- [91] Yang S, Ling X, Du P (2018) Elastic and plastic deformation behavior analysis in small punch test for mechanical properties evaluation. *J Cent South Univ* 25:747–753. <https://doi.org/10.1007/s11771-018-3779-7>
- [92] Altstadt E, Houska M, Simonovski I, Bruchhausen M, Holmström S, Lacalle R (2018) On the estimation of ultimate tensile stress from small punch testing. *Int J Mech Sci* 136:85–93. <https://doi.org/10.1016/j.ijmecsci.2017.12.016>
- [93] Moreno MF, Bertolino G, Yawny A (2016) The significance of specimen displacement definition on the mechanical properties derived from Small Punch Test. *Mater Des* 95:623–631. <https://doi.org/10.1016/j.matdes.2016.01.148>
- [94] Rasche S, Kuna M (2015) Improved small punch testing and parameter identification of ductile to brittle materials. *Int J Pressure Vessel Pip* 125:23–34. <https://doi.org/10.1016/j.ijpvp.2014.09.001>
- [95] Simonovski I, Holmström S, Bruchhausen M (2017) Small punch tensile testing of curved specimens: Finite element analysis and experiment. *Int J Mech Sci* 120:204–213. <https://doi.org/10.1016/j.ijmecsci.2016.11.029>
- [96] Haroush S, Priel E, Moreno D, Busiba A, Silverman I, Turgeman A, Shneck R, Gelbstein Y (2015) Evaluation of the mechanical properties of SS-316L thin foils by small punch testing and finite element analysis. *Mater Des* 83:75–84. <https://doi.org/10.1016/j.matdes.2015.05.049>
- [97] Priel E, Mittelman B, Haroush S, Turgeman A, Shneck R, Gelbstein Y (2018) Estimation of yield and ultimate stress using the small punch test method applied to non-standard specimens: a computational study validated by experiments. *Int J Mech Sci* 135:484–498. <https://doi.org/10.1016/j.ijmecsci.2017.11.040>
- [98] García TE, Rodríguez C, Belzunce FJ, Cuesta II (2015) Development of a new methodology for estimating the CTOD of structural steels using the small punch test. *Eng*

- Fail Anal 50:88–99. <https://doi.org/10.1016/j.engfailanal.2015.01.011>
- [99] Alegre JM, Lacalle R, Cuesta II, Álvarez JA (2016) Different methodologies to obtain the fracture properties of metallic materials using pre-notched small punch test specimens. *Theor Appl Fract Mech* 86:11–18. <https://doi.org/10.1016/j.tafmec.2016.09.006>
- [100] Hurst R, Li Y, Turba K (2019) Determination of fracture toughness from the small punch test using circular notched specimens. *Theor Appl Fract Mech* 103:102238. <https://doi.org/10.1016/j.tafmec.2019.102238>
- [101] Cuesta II, Willig A, Díaz A, Martínez-Pañeda E, Alegre JM (2019) Pre-notched dog bone small punch specimens for the estimation of fracture properties. *Eng Fail Anal* 96:236–240. <https://doi.org/10.1016/j.engfailanal.2018.10.012>
- [102] Peng J, Vijayanand VD, Knowles D, Truman C, Mostafavi M (2021) The sensitivity ranking of ductile material mechanical properties, geometrical factors, friction coefficients and damage parameters for small punch test. *Int J Pressure Vessels Pip* 193:104468. <https://doi.org/10.1016/j.ijvp.2021.104468>
- [103] Otroshi M, Meschut G (2022) Influence of cutting clearance and punch geometry on the stress state in small punch test. *Eng Fail Anal* 136:106183. <https://doi.org/10.1016/j.engfailanal.2022.106183>
- [104] Andrés D, Dymáček P (2016) Study of the upper die clamping conditions in the small punch test. *Theor Appl Fract Mech* 86:117–123. <https://doi.org/10.1016/j.tafmec.2016.07.012>
- [105] Prakash RV, Arunkumar S (2015) Evaluation of damage in materials due to fatigue cycling through static and cyclic small punch testing. In: Sokolov MA, Lucon E (eds) *Small specimen test techniques: 6th volume*. ASTM International, pp 168–186
- [106] Yang S, Zhou J, Ling X, Yang Z (2012) Effect of geometric factors and processing parameters on plastic damage of SUS304 stainless steel by small punch test. *Mater Des* 41:447–452. <https://doi.org/10.1016/j.matdes.2012.05.029>
- [107] Sánchez-Ávila D, Orozco-Caballero A, Martínez E, Portolés L, Barea R, Carreño F (2021) High-accuracy compliance correction for nonlinear mechanical testing: Improving Small Punch Test characterization. *Nucl Mater Energy* 26:100914. <https://doi.org/10.1016/j.nme.2021.100914>
- [108] Vijayanand VD, Mokhtarishirazabad M, Peng J, Wang Y, Gorley M, Knowles DM, Mostafavi M (2020) A novel methodology for estimating tensile properties in a small punch test employing in-situ DIC based deflection mapping. *J Nucl Mater* 538:152260. <https://doi.org/10.1016/j.jnucmat.2020.152260>
- [109] Pham HT, Iwamoto T (2018) An evaluation of fracture properties of type-304 austenitic stainless steel at high deformation rate using the small punch test. *Int J Mech Sci* 144:249–261. <https://doi.org/10.1016/j.ijmecsci.2018.05.056>
- [110] Cao B, Yoshida S, Iwamoto T, Pham HT (2021) Development of impact small punch test for investigating energy absorption. *Int J Mech Sci* 208:106675. <https://doi.org/10.1016/j.ijmecsci.2021.106675>
- [111] Calaf-Chica J, Bravo Díez PM, Preciado Calzada M, Bal-lorca-Juez D (2019) A systematic FEM analysis of the influence of mechanical properties in the reliability of the correlation methods in the small punch test. *Int J Mech Sci* 153–154:299–309. <https://doi.org/10.1016/j.ijmecsci.2019.02.013>
- [112] Chica JC, Bravo Díez PM, Preciado Calzada M (2017) Improved correlation for elastic modulus prediction of metallic materials in the Small Punch Test. *Int J Mech Sci* 134:112–122. <https://doi.org/10.1016/j.ijmecsci.2017.10.006>
- [113] Janča A, Siegl J, Haušild P (2016) Small punch test evaluation methods for material characterisation. *J Nucl Mater* 481:201–213. <https://doi.org/10.1016/j.jnucmat.2016.09.015>
- [114] García TE, Rodríguez C, Belzunce FJ, Suárez C (2014) Estimation of the mechanical properties of metallic materials by means of the small punch test. *J Alloy Compd* 582:708–717. <https://doi.org/10.1016/j.jallcom.2013.08.009>
- [115] Moreno MF (2018) Effects of thickness specimen on the evaluation of relationship between tensile properties and small punch testing parameters in metallic materials. *Mater Des* 157:512–522. <https://doi.org/10.1016/j.matdes.2018.07.065>
- [116] Cuesta II, Alegre JM, Lorenzo M (2014) Influence of strain state in mechanical behaviour of aluminium alloys using the Small Punch Test. *Mater Des* 54:291–294. <https://doi.org/10.1016/j.matdes.2013.08.038>
- [117] Kumar P, Chattopadhyay J, Dutta BK (2016) On the correlation between minimum thickness and central deflection during small punch test. *J Nucl Mater* 475:37–45. <https://doi.org/10.1016/j.jnucmat.2016.03.012>
- [118] Patel P, Patel BK (2022) The small punch test a viable alternate for in-service components preserved strength estimation. *J Inst Eng India Ser C* 103:121–133. <https://doi.org/10.1007/s40032-021-00728-1>
- [119] Calaf-Chica J, Bravo Díez PM, Preciado Calzada M, Garcia-Tarrago M-J (2020) Optimization of the t/10 offset

- correlation method to obtain the yield strength with the Small Punch Test. *J Nucl Mater* 534:152177. <https://doi.org/10.1016/j.jnucmat.2020.152177>
- [120] Calaf Chica J, Bravo Díez PM, Preciado Calzada M (2018) Development of an improved prediction method for the yield strength of steel alloys in the Small Punch Test. *Mater Des* 148:153–166. <https://doi.org/10.1016/j.matdes.2018.03.064>
- [121] Chen H, Cai L (2019) An elastoplastic energy model for predicting the deformation behaviors of various structural components. *Appl Math Model* 68:405–421. <https://doi.org/10.1016/j.apm.2018.11.024>
- [122] Chen H, Cai L (2019) A universal elastic-plastic model correlating load-displacement relation and constitutive parameters for typical testing components. *Results Phys* 13:102230. <https://doi.org/10.1016/j.rinp.2019.102230>
- [123] Zhang X, Zhang C, Ding Z, Chen Y, Zhang L (2020) Quantification of the constitutive relationship of high-energy heavy-ion irradiated SS316L using the small punch test. *J Nucl Mater* 531:152014. <https://doi.org/10.1016/j.jnucmat.2020.152014>
- [124] Zhong J, Xu T, Guan K, Szpunar J (2019) A procedure for predicting strength properties using small punch test and finite element simulation. *Int J Mech Sci* 152:228–235. <https://doi.org/10.1016/j.ijmecsci.2019.01.006>
- [125] Yang S, Ling X, Xue L (2018) Application of small punch test to investigate mechanical behaviours and deformation characteristics of Incoloy800H. *J Alloy Compd* 765:497–504. <https://doi.org/10.1016/j.jallcom.2018.06.243>
- [126] Calaf-Chica J, Bravo Díez PM, Preciado Calzada M (2020) Influence of the material anisotropy in the estimation of the yield strength with the Small Punch Test. *Fusion Eng Des* 160:112019. <https://doi.org/10.1016/j.fusengdes.2020.112019>
- [127] Calaf-Chica J, Sánchez Palomar M, Bravo Díez PM, Preciado Calzada M (2021) Deviations in yield and ultimate tensile strength estimation with the Small Punch Test: numerical analysis of pre-straining and Bauschinger effect influence. *Mech Mater* 153:103696. <https://doi.org/10.1016/j.mechmat.2020.103696>
- [128] Cuesta II, Alegre JM (2012) Hardening evaluation of stamped aluminium alloy components using the Small Punch Test. *Eng Fail Anal* 26:240–246. <https://doi.org/10.1016/j.engfailanal.2012.06.004>
- [129] Xue L, Ling X, Yang S (2019) Mechanical behaviour and strain rate sensitivity analysis of TA2 by the small punch test. *Theor Appl Fract Mech* 99:9–17. <https://doi.org/10.1016/j.tafmec.2018.11.002>
- [130] Lotfolahpour A, Soltani N, Ganjiani M, Baharlouei D (2018) Parameters identification and validation of plastic-damage model of 304 stainless steel by small punch test at ambient temperature. *Eng Fract Mech* 200:64–74. <https://doi.org/10.1016/j.engfracmech.2018.07.007>
- [131] Cuesta II, Alegre JM (2014) Influence of biaxial pre-deformation on fracture properties using pre-notched small punch specimens. *Eng Fract Mech* 131:1–8. <https://doi.org/10.1016/j.engfracmech.2014.10.001>
- [132] Holmström S, Simonovski I, Baraldi D, Bruchhausen M, Altstadt E, Delville R (2019) Developments in the estimation of tensile strength by small punch testing. *Theor Appl Fract Mech* 101:25–34. <https://doi.org/10.1016/j.tafmec.2019.01.020>
- [133] Jeffs S, Douglas R, Beard W, Coleman M, Adams J, Jones T, Poole D, Lancaster R (2022) Characterising the high temperature tensile behaviour of laser powder bed fused duplex stainless steel 2205 using the small punch test. *Mater Charact* 189:111953. <https://doi.org/10.1016/j.matchar.2022.111953>
- [134] Lee J-M, Hwang J-H, Kim Y-J, Kim J-W (2021) Predicting ductile fracture of cracked pipes using small punch test data. *Eur J Mech A Solids* 87:104211. <https://doi.org/10.1016/j.euromechsol.2021.104211>
- [135] Liu H, Ma J, Tang A, Tang J, Zhang C, Zhang L, Shen Y (2020) True stress-strain curve extraction from ion-irradiated materials via small tensile, small punch and nanoindentation tests: method development and accuracy/consistency verification. *Nucl Fusion* 60:56012. <https://doi.org/10.1088/1741-4326/ab7c2a>
- [136] Li K, Peng J, Zhou C (2018) Construction of whole stress-strain curve by small punch test and inverse finite element. *Results Phys* 11:440–448. <https://doi.org/10.1016/j.rinp.2018.09.024>
- [137] Martínez-Pañeda E, Cuesta II, Peñuelas I, Díaz A, Alegre JM (2016) Damage modeling in small punch test specimens. *Theor Appl Fract Mech* 86:51–60. <https://doi.org/10.1016/j.tafmec.2016.09.002>
- [138] Kubík P, Šebek F, Petruška J, Hůlka J, Park N, Huh H (2018) Comparative investigation of ductile fracture with 316L austenitic stainless steel in small punch tests: Experiments and simulations. *Theor Appl Fract Mech* 98:186–198. <https://doi.org/10.1016/j.tafmec.2018.10.005>
- [139] Simonovski I, Holmström S, Baraldi D, Delville R (2020) Investigation of cracking in small punch test for semi-brittle materials. *Theor Appl Fract Mech* 108:102646. <https://doi.org/10.1016/j.tafmec.2020.102646>
- [140] Šebek F, Park N, Kubík P, Petruška J, Zapletal J (2019) Ductile fracture predictions in small punch testing of cold-

- rolled aluminium alloy. *Eng Fract Mech* 206:509–525. <https://doi.org/10.1016/j.engfracmech.2018.11.045>
- [141] Martínez-Pañeda E, García TE, Rodríguez C (2016) Fracture toughness characterization through notched small punch test specimens. *Mater Sci Eng A-Struct* 657:422–430. <https://doi.org/10.1016/j.msea.2016.01.077>
- [142] Sun Q, Lu Y, Chen J (2020) Identification of material parameters of a shear modified GTN damage model by small punch test. *Int J Fract* 222:25–35. <https://doi.org/10.1007/s10704-020-00428-4>
- [143] Soyarslan C, Gülçimen B, Bargmann S, Hähner P (2016) Modeling of fracture in small punch tests for small- and large-scale yielding conditions at various temperatures. *Int J Mech Sci* 106:266–285. <https://doi.org/10.1016/j.ijmecsci.2015.12.007>
- [144] Jeon J-Y, Kim Y-J, Lee S-Y, Kim J-W (2016) Extracting ductile fracture toughness from small punch test data using numerical modeling. *Int J Pressure Vessel Pip* 139–140:204–219. <https://doi.org/10.1016/j.ijpvp.2016.02.011>
- [145] Arunkumar S (2020) Overview of small punch test. *Met Mater Int* 26:719–738. <https://doi.org/10.1007/s12540-019-00454-5>
- [146] Cheng Z, Sun J, Tai P, Zhang L, Wei Y, Chang H, Thuku R, Gichuhi KM (2021) Comparative study between small punch tests and finite element analysis of miniature steel specimens. *J Mater Eng Perform* 30:9094–9107. <https://doi.org/10.1007/s11665-021-06098-0>
- [147] Song M, Guan K, Qin W, Szpunar JA, Chen J (2014) Size effect criteria on the small punch test for AISI 316L austenitic stainless steel. *Mater Sci Eng A Struct* 606:346–353. <https://doi.org/10.1016/j.msea.2014.03.098>
- [148] Wang W, Xu T, Zhong J, Guan K, Shang Y, Zhang X (2022) Specimen size effect on evaluation of strength properties of 3Cr1MoV and Incoloy 800H using small punch test. *Mater Sci Eng A Struct* 832:142400. <https://doi.org/10.1016/j.msea.2021.142400>
- [149] Seupel A, Hütter G, Kuna M (2020) On the identification and uniqueness of constitutive parameters for a non-local GTN-model. *Eng Fract Mech* 229:106817. <https://doi.org/10.1016/j.engfracmech.2019.106817>
- [150] Altstadt E, Ge HE, Kuksenko V, Serrano M, Houska M, Lasan M, Bruchhausen M, Lapetite J-M, Dai Y (2016) Critical evaluation of the small punch test as a screening procedure for mechanical properties. *J Nucl Mater* 472:186–195. <https://doi.org/10.1016/j.jnucmat.2015.07.029>
- [151] Guan K, Xu T, Zhang X, Wang Z (2013) Effect of microdefects on load-deflection of small punch test by experimental investigation and finite element analysis. *Int J Pressure Vessels Pip* 110:14–16. <https://doi.org/10.1016/j.ijpvp.2013.04.016>
- [152] Yang S, Ling X, Yang X, Lu S (2014) Mechanical properties estimation of materials with different grain sizes by small punch test at elevated temperature. In: ASME 2014 pressure vessels and piping conference, Volume 6B: Materials and Fabrication.
- [153] Moreno-Valle EC, Pachla W, Kulczyk M, Savoini B, Monge MA, Ballesteros C, Sabirov I (2013) Anisotropy of uni-axial and bi-axial deformation behavior of pure Titanium after hydrostatic extrusion. *Mater Sci Eng A Struct* 588:7–13. <https://doi.org/10.1016/j.msea.2013.08.044>
- [154] Rezaei A, Rezaeian A, Kermanpur A, Badrossamay M, Foroozmehr E, Marashi M, Foroozmehr A, Han J (2020) Microstructural and mechanical anisotropy of selective laser melted IN718 superalloy at room and high temperatures using small punch test. *Mater Charact* 162:110200. <https://doi.org/10.1016/j.matchar.2020.110200>
- [155] Song M, Guan K, Qin W, Szpunar JA (2012) Comparison of mechanical properties in conventional and small punch tests of fractured anisotropic A350 alloy forging flange. *Nucl Eng Des* 247:58–65. <https://doi.org/10.1016/j.nucengdes.2012.03.023>
- [156] Rodríguez C, Fernández M, Cabezas JG, García TE, Belzunce FJ (2016) The use of the small punch test to solve practical engineering problems. *Theor Appl Fract Mech* 86:109–116. <https://doi.org/10.1016/j.tafmec.2016.08.021>
- [157] Gülçimen B, Durmuş A, Ülkü S, Hurst RC, Turba K, Hähner P (2013) Mechanical characterisation of a P91 weldment by means of small punch fracture testing. *Int J Pressure Vessels Pip* 105–106:28–35. <https://doi.org/10.1016/j.ijpvp.2013.02.005>
- [158] Fan Y, Yang BL, Liu TG, Lu YH (2020) Effect of inhomogeneous microstructure on the deformation and fracture mechanisms of 316LN stainless steel multi-pass weld joint using small punch test. *J Nucl Mater* 538:152239. <https://doi.org/10.1016/j.jnucmat.2020.152239>
- [159] Gao T, Ying L, Hu P, Han X, Rong H, Wu Y, Sun J (2020) Investigation on mechanical behavior and plastic damage of AA7075 aluminum alloy by thermal small punch test: Experimental trials, numerical analysis. *J Manuf Process* 50:1–16. <https://doi.org/10.1016/j.jmapro.2019.12.012>
- [160] Zhou X, Pan W, MacKenzie D, Fu R (2014) Identifying plastic properties of friction stir-welded material by small punch beam test. *Proc Inst Mech Eng Part L-J Mater* 228:201–207. <https://doi.org/10.1177/1464420713480021>
- [161] Banafshi A, Fereshteh-Saniee F (2018) Shear behavior of AZ80 Mg alloy using experimental, theoretical and numerical techniques. *Trans Nonferrous Met Soc China*

- 28:2427–2439. [https://doi.org/10.1016/S1003-6326\(18\)64889-7](https://doi.org/10.1016/S1003-6326(18)64889-7)
- [162] Zhuang F-K, Tu S-T (2015) Sensitivity analysis of ball punch geometry for small punch testing. *Procedia Eng* 130:1019–1028. <https://doi.org/10.1016/j.proeng.2015.12.255>
- [163] Sellamuthu P, Collins PK, Hodgson PD, Stanford N (2013) Correlation of tensile test properties with those predicted by the shear punch test. *Mater Des* 47:258–266. <https://doi.org/10.1016/j.matdes.2012.11.057>
- [164] Lancaster RJ, Jeffs SP, Haigh BJ, Barnard NC (2022) Derivation of material properties using small punch and shear punch test methods. *Mater Des* 215:110473. <https://doi.org/10.1016/j.matdes.2022.110473>
- [165] Ansarian I, Shaeri MH, Ebrahimi M, Minárik P, Bartha K (2019) Microstructure evolution and mechanical behaviour of severely deformed pure titanium through multi directional forging. *J Alloy Compd* 776:83–95. <https://doi.org/10.1016/j.jallcom.2018.10.196>
- [166] Rabenberg EM, Jaques BJ, Sencer BH, Garner FA, Freyer PD, Okita T, Butt DP (2014) Mechanical behavior of AISI 304SS determined by miniature test methods after neutron irradiation to 28dpa. *J Nucl Mater* 448:315–324. <https://doi.org/10.1016/j.jnucmat.2014.02.018>
- [167] Abedi HR, Zarei-Hanzaki A, Bagherzadeh Biucki M, Emamy M (2014) Evaluating the room temperature mechanical properties of age hardened AZ80 magnesium alloy using shear punch testing method. *Mater Sci Eng A Struct* 606:360–369. <https://doi.org/10.1016/j.msea.2014.03.106>
- [168] Mahmudi R, Alizadeh R, Azhari S (2013) Strain rate sensitivity of equal-channel angularly pressed Sn–5Sb alloy determined by shear punch test. *Mater Lett* 97:44–46. <https://doi.org/10.1016/j.matlet.2013.01.078>
- [169] Esfandyarpour MJ, Alizadeh R, Mahmudi R (2019) Applicability of shear punch testing to the evaluation of hot tensile deformation parameters and constitutive analyses. *J Mater Res Technol-JMRT* 8:996–1002. <https://doi.org/10.1016/j.jmrt.2018.02.014>
- [170] Wilcox H, Lewis B, Styman P (2021) Evaluation of the mechanical properties of precipitation-hardened martensitic steel 17–4PH using small and shear punch testing. *J Mater Eng Perform* 30:4206–4216. <https://doi.org/10.1007/s11665-021-05756-7>
- [171] Zergani A, Mirzadeh H, Mahmudi R (2020) Evolutions of mechanical properties of AISI 304L stainless steel under shear loading. *Mater Sci Eng A-Struct* 791:139667. <https://doi.org/10.1016/j.msea.2020.139667>
- [172] Nakamura N, Mori K, Okada H, Abe Y (2021) Punching test for estimating tensile strength and total elongation of steel sheets. *Int J Adv Manuf Technol* 114:1847–1858. <https://doi.org/10.1007/s00170-021-06898-7>
- [173] Monajati H, Zoghلامي M, Tongne A, Jahazi M (2020) Assessing microstructure-local mechanical properties in friction atir welded 6082–T6 aluminum alloy. *Metals* 10:1244. <https://doi.org/10.3390/met10091244>
- [174] Hornbuckle BC, Murdoch HA, Roberts AJ, Kecskes LJ, Tschopp MA, Doherty KJ, Yu JH, Darling KA (2017) Property mapping of friction stir welded Al-2139 T8 plate using site specific shear punch testing. *Mater Sci Eng A Struct* 682:192–201. <https://doi.org/10.1016/j.msea.2016.11.032>
- [175] Ding R, Guo C, Guo S (2013) Assessment of anisotropic tensile strength using a modified shear punch test for Cu–Cr–Zr alloy processed by severe plastic deformation. *Mater Sci Eng A Struct* 587:320–327. <https://doi.org/10.1016/j.msea.2013.09.003>
- [176] Arunkumar S (2018) A review of indentation theory. *Mater Today Proc* 5:23664–23673. <https://doi.org/10.1016/j.matpr.2018.10.156>
- [177] GB/T 37782-2019 Metallic materials —Indentation test— Determination of strength, hardness and stress-strain curve
- [178] ISO 14577-1:2015 Metallic materials—instrumented indentation test for hardness and materials parameters— part 1: test method
- [179] ASTM E2546-15 Standard practice for instrumented indentation testing
- [180] GB/T 21838.1-2019 Metallic materials—instrumented indentation test for hardness and materials parameters— part 1: test method:
- [181] GB/T 22458–2008 General rules of instrumented nanoindentation test :
- [182] Yang F, Li JC (2013) Impression test—a review. *Mater Sci Eng R-Rep* 74:233–253. <https://doi.org/10.1016/j.mser.2013.06.002>
- [183] Zhang T (2013) Micro/nano mechanics testing technology: measurement, analysis, application and standardization of instrumented indentation test. Science Press, Beijing
- [184] Ma L, Low S, Song J (2014) A method to determine the spherical indentation contact boundary diameter in elastic–plastic materials. *Mech Mater* 69:213–226. <https://doi.org/10.1016/j.mechmat.2013.11.001>
- [185] N’jock MY, Chicot D, Ndjaka JM, Lesage J, Decoopman X, Roudet F, Mejjias A (2015) A criterion to identify sinking-in and piling-up in indentation of materials. *Int J Mech Sci* 90:145–150. <https://doi.org/10.1016/j.ijmecsci.2014.11.008>
- [186] Karthik V, Visweswaran P, Bhushan A, Pawaskar DN, Kasiviswanathan KV, Jayakumar T, Raj B (2012) Finite element analysis of spherical indentation to study pile-up/

- sink-in phenomena in steels and experimental validation. *Int J Mech Sci* 54:74–83. <https://doi.org/10.1016/j.ijmecsci.2011.09.009>
- [187] Phadikar JK, Bogetti TA, Karlsson AM (2013) On the uniqueness and sensitivity of indentation testing of isotropic materials. *Int J Solids Struct* 50:3242–3253. <https://doi.org/10.1016/j.ijsolstr.2013.05.028>
- [188] Pathak S, Kalidindi SR (2015) Spherical nanoindentation stress–strain curves. *Mater Sci Eng R Rep* 91:1–36. <https://doi.org/10.1016/j.mser.2015.02.001>
- [189] Phani PS, Oliver WC, Pharr GM (2020) Understanding and modeling plasticity error during nanoindentation with continuous stiffness measurement. *Mater Des* 194:108923. <https://doi.org/10.1016/j.matdes.2020.108923>
- [190] Calle M, Mazzariol LM, Alves M (2018) Strain rate sensitivity assessment of metallic materials by mechanical indentation tests. *Mater Sci Eng A Struct* 725:274–282. <https://doi.org/10.1016/j.msea.2018.04.023>
- [191] Ito K, Arai M (2021) Simple estimation method for strain rate sensitivity based on the difference between the indentation sizes formed by spherical-shaped impactors. *Int J Mech Sci* 189:106007. <https://doi.org/10.1016/j.ijmecsci.2020.106007>
- [192] Wheeler JM, Dean J, Clyne TW (2019) Nano-impact indentation for high strain rate testing: the influence of rebound impacts. *Extreme Mech Lett* 26:35–39. <https://doi.org/10.1016/j.eml.2018.11.005>
- [193] Saxena A, Dwivedi SP, Kumaraswamy A, Srivastava AK, Maurya NK (2022) Influence of SD effect on Johnson-Cook hardening constitutive material model: Numerical and experimental investigation for armor steel. *Mech Adv Mater Struct* 29:285–302. <https://doi.org/10.1080/15376494.2020.1765266>
- [194] Zehnder C, Peltzer J-N, Gibson JS-L, Korte-Kerzel S (2018) High strain rate testing at the nano-scale: a proposed methodology for impact nanoindentation. *Mater Des* 151:17–28. <https://doi.org/10.1016/j.matdes.2018.04.045>
- [195] Chang C, Garrido MA, Ruiz-Hervias J, Rodríguez J (2017) On the possibility of reducing the pile-up effect on the Berkovich instrumented indentation tests. *Int J Mech Sci* 121:181–186. <https://doi.org/10.1016/j.ijmecsci.2017.01.008>
- [196] Liu M, Lu C, Tieu K, Yu H (2014) Numerical comparison between Berkovich and conical nano-indentations: mechanical behaviour and micro-texture evolution. *Mater Sci Eng A Struct* 619:57–65. <https://doi.org/10.1016/j.msea.2014.09.034>
- [197] Yetna N’Jock M, Roudet F, Idriss M, Bartier O, Chicot D (2016) Work-of-indentation coupled to contact stiffness for calculating elastic modulus by instrumented indentation. *Mech Mater* 94:170–179. <https://doi.org/10.1016/j.mechmat.2015.12.003>
- [198] Roa S, Sirena M (2021) A finite element analysis of conical indentation in elastic-plastic materials: on strain energy based strategies for an area-independent determination of solids mechanical properties. *Int J Mech Sci* 207:106651. <https://doi.org/10.1016/j.ijmecsci.2021.106651>
- [199] Hemmouche L, Chicot D, Amrouche A, Iost A, Belouchrani MA, Decoopman X, Louis G, Puchi-Cabrera ES (2013) An analysis of the elastic properties of a porous aluminium oxide film by means of indentation techniques. *Mater Sci Eng A-Struct* 585:155–164. <https://doi.org/10.1016/j.msea.2013.07.054>
- [200] Cagliero R, Barbato G, Maizza G, Genta G (2015) Measurement of elastic modulus by instrumented indentation in the macro-range: uncertainty evaluation. *Int J Mech Sci* 101–102:161–169. <https://doi.org/10.1016/j.ijmecsci.2015.07.030>
- [201] Zorzi JE, Perottoni CA (2013) Estimating Young’s modulus and Poisson’s ratio by instrumented indentation test. *Mater Sci Eng A Struct* 574:25–30. <https://doi.org/10.1016/j.msea.2013.03.008>
- [202] Yetna N’Jock M, Chicot D, Decoopman X, Lesage J, Ndjaka JM, Pertuz A (2013) Mechanical tensile properties by spherical macroindentation using an indentation strain-hardening exponent. *Int J Mech Sci* 75:257–264. <https://doi.org/10.1016/j.ijmecsci.2013.07.008>
- [203] Moussa C, Hernot X, Bartier O, Delattre G, Mauvoisin G (2014) Identification of the hardening law of materials with spherical indentation using the average representative strain for several penetration depths. *Mater Sci Eng A Struct* 606:409–416. <https://doi.org/10.1016/j.msea.2014.03.123>
- [204] Goto K, Watanabe I, Ohmura T (2019) Determining suitable parameters for inverse estimation of plastic properties based on indentation marks. *Int J Plast* 116:81–90. <https://doi.org/10.1016/j.ijplas.2018.12.007>
- [205] Ma ZS, Zhou YC, Long SG, Zhong XL, Lu C (2012) Characterization of stress-strain relationships of elastoplastic materials: an improved method with conical and pyramidal indenters. *Mech Mater* 54:113–123. <https://doi.org/10.1016/j.mechmat.2012.07.006>
- [206] Patel DK, Kalidindi SR (2016) Correlation of spherical nanoindentation stress-strain curves to simple compression stress-strain curves for elastic-plastic isotropic materials using finite element models. *Acta Mater* 112:295–302. <https://doi.org/10.1016/j.actamat.2016.04.034>
- [207] Campbell JE, Thompson RP, Dean J, Clyne TW (2019) Comparison between stress-strain plots obtained from indentation plastometry, based on residual indent profiles,

- and from uniaxial testing. *Acta Mater* 168:87–99. <https://doi.org/10.1016/j.actamat.2019.02.006>
- [208] Dean J, Clyne TW (2017) Extraction of plasticity parameters from a single test using a spherical indenter and FEM modelling. *Mech Mater* 105:112–122. <https://doi.org/10.1016/j.mechmat.2016.11.014>
- [209] Meng L, Breitenkopf P, Le Quilliec G (2017) An insight into the identifiability of material properties by instrumented indentation test using manifold approach based on P-h curve and imprint shape. *Int J Solids Struct* 106–107:13–26. <https://doi.org/10.1016/j.ijsolstr.2016.12.002>
- [210] Li Y, Stevens P, Sun M, Zhang C, Wang W (2016) Improvement of predicting mechanical properties from spherical indentation test. *Int J Mech Sci* 117:182–196. <https://doi.org/10.1016/j.ijmecsci.2016.08.019>
- [211] Pham T-H, Kim JJ, Kim S-E (2015) Estimating constitutive equation of structural steel using indentation. *Int J Mech Sci* 90:151–161. <https://doi.org/10.1016/j.ijmecsci.2014.11.007>
- [212] Kang JJ, Becker AA, Wen W, Sun W (2018) Extracting elastic-plastic properties from experimental loading-unloading indentation curves using different optimization techniques. *Int J Mech Sci* 144:102–109. <https://doi.org/10.1016/j.ijmecsci.2018.05.043>
- [213] Kang S-K, Kim Y-C, Kim K-H, Kim J-Y, Kwon D (2013) Extended expanding cavity model for measurement of flow properties using instrumented spherical indentation. *Int J Plast* 49:1–15. <https://doi.org/10.1016/j.ijplas.2013.02.014>
- [214] Zhang T, Wang S, Wang W (2018) A constitutive model independent analytical method in determining the tensile properties from incremental spherical indentation tests (ISITs). *Int J Mech Sci* 148:9–19. <https://doi.org/10.1016/j.ijmecsci.2018.08.010>
- [215] Donohue BR, Ambrus A, Kalidindi SR (2012) Critical evaluation of the indentation data analyses methods for the extraction of isotropic uniaxial mechanical properties using finite element models. *Acta Mater* 60:3943–3952. <https://doi.org/10.1016/j.actamat.2012.03.034>
- [216] Samal MK, Syed A, Khatri RN, Chattopadhyay J (2021) Study of plastically deformed region underneath the ball in indentation tests and evaluation of mechanical properties of materials through finite element simulation and a hybrid algorithm. *Proc Inst Mech Eng Part C J Mech* 235:108–121. <https://doi.org/10.1177/0954406220932947>
- [217] Goto K, Watanabe I, Ohmura T (2020) Inverse estimation approach for elastoplastic properties using the load-displacement curve and pile-up topography of a single Berkovich indentation. *Mater Des* 194:108925. <https://doi.org/10.1016/j.matdes.2020.108925>
- [218] Zhang T, Wang S, Wang W (2020) An energy-based method for flow property determination from a single-cycle spherical indentation test (SIT). *Int J Mech Sci* 171:105369. <https://doi.org/10.1016/j.ijmecsci.2019.105369>
- [219] Chen H, Cai L (2016) Theoretical model for predicting uniaxial stress-strain relation by dual conical indentation based on equivalent energy principle. *Acta Mater* 121:181–189. <https://doi.org/10.1016/j.actamat.2016.09.008>
- [220] Xia J, Won C, Kim H, Lee W, Yoon J (2022) Artificial neural networks for predicting plastic anisotropy of sheet metals based on indentation test. *Materials* 15:1714. <https://doi.org/10.3390/ma15051714>
- [221] Wang M, Wu J, Zhan X, Guo R, Hui Y, Fan H (2016) On the determination of the anisotropic plasticity of metal materials by using instrumented indentation. *Mater Des* 111:98–107. <https://doi.org/10.1016/j.matdes.2016.08.076>
- [222] Wang M, Gao L, Cao K, Wu J, Wang W (2021) A Bayesian inverse approach to measure the anisotropic plasticity properties of materials using spherical indentation experiment. *Measurement* 171:108812. <https://doi.org/10.1016/j.measurement.2020.108812>
- [223] Zhan X, Wu J, Wu H, Wang M, Hui Y, Shang Q, Ren Y (2018) A new modified ECM approach on the identification of plastic anisotropic properties by spherical indentation. *Mater Des* 139:392–408. <https://doi.org/10.1016/j.matdes.2017.11.015>
- [224] Lee JH, Gao YF, Johans KE, Pharr GM (2012) Cohesive interface simulations of indentation cracking as a fracture toughness measurement method for brittle materials. *Acta Mater* 60:5448–5467. <https://doi.org/10.1016/j.actamat.2012.07.011>
- [225] Zhang T, Wang S, Wang W (2019) A comparative study on fracture toughness calculation models in spherical indentation tests (SITs) for ductile metals. *Int J Mech Sci* 160:114–128. <https://doi.org/10.1016/j.ijmecsci.2019.06.035>
- [226] Hwang Y, Marimuthu KP, Kim N, Lee C, Lee H (2021) Extracting plastic properties from in-plane displacement data of spherical indentation imprint. *Int J Mech Sci* 197:106291. <https://doi.org/10.1016/j.ijmecsci.2021.106291>
- [227] Mostafavi M, Collins DM, Cai B, Bradley R, Atwood RC, Reinhard C, Jiang X, Galano M, Lee PD, Marrow TJ (2015) Yield behavior beneath hardness indentations in ductile metals, measured by three-dimensional computed X-ray tomography and digital volume correlation. *Acta Mater* 82:468–482. <https://doi.org/10.1016/j.actamat.2014.08.046>

- [228] Chunyu Z, Yulong Z, Yobuin C, Nanfeng C, Lei C (2017) Understanding indentation-induced elastic modulus degradation of ductile metallic materials. *Mater Sci Eng A Struct* 696:445–452. <https://doi.org/10.1016/j.msea.2017.04.094>
- [229] Zhang C, Xiao W (2015) Shear-driven damage of ductile metals induced by indentation load. *Philos Mag Lett* 95:401–407. <https://doi.org/10.1080/09500839.2015.1081299>
- [230] Zou B, Guan KS, Wu SB (2016) Determination of area reduction rate by continuous ball indentation test. *Int J Pressure Vessels Pip* 139–140:220–227. <https://doi.org/10.1016/j.ijpvp.2016.02.023>
- [231] Chen Y, Zhang C, Varé C (2017) An extended GTN model for indentation-induced damage. *Comput Mater Sci* 128:229–235. <https://doi.org/10.1016/j.commatsci.2016.11.043>
- [232] Li J, Li F, Ma X, Wang Q, Dong J, Yuan Z (2015) A strain-dependent ductile damage model and its application in the derivation of fracture toughness by micro-indentation. *Mater Des* 67:623–630. <https://doi.org/10.1016/j.matdes.2014.11.010>
- [233] Xue FM, Li FG, Li J, He M (2012) Strain energy density method for estimating fracture toughness from indentation test of 0Cr12Mn5Ni4Mo3Al steel with Berkovich indenter. *Theor Appl Fract Mech* 61:66–72. <https://doi.org/10.1016/j.tafmec.2012.08.008>
- [234] Sun Z, Li F, Ma X, Cao J, Li J, Hou J, Wang W (2019) Damage controlled by brittle particles crush in AA7075-T6 beneath spherical indenter. *Eng Fract Mech* 212:28–40. <https://doi.org/10.1016/j.engfracmech.2019.03.017>
- [235] Ghosh S, Das G (2012) Effect of pre-strain on the indentation fracture toughness of high strength low alloy steel by means of continuum damage mechanics. *Eng Fract Mech* 79:126–137. <https://doi.org/10.1016/j.engfracmech.2011.1.0.008>
- [236] Wu SJ, Qu RT, Liu ZC, Li HF, Wang XD, Tan CW, Zhang P, Zhang ZF (2021) Locating the optimal microstructural state against dynamic perforation by evaluating the strain-rate dependences of strength and hardness. *Int J Impact Eng* 152:103856. <https://doi.org/10.1016/j.ijimpeng.2021.103856>
- [237] Chen G, Zhong J, Zhang X, Guan K, Wang Q, Shi J (2021) Estimation of tensile strengths of metals using spherical indentation test and database. *Int J Pressure Vessels Pip* 189:104284. <https://doi.org/10.1016/j.ijpvp.2020.104284>
- [238] Nguyen N-V, Kim S-E (2020) Experimental study to investigate microstructure and continuous strain rate sensitivity of structural steel weld zone using nanoindentation. *Int J Mech Sci* 174:105482. <https://doi.org/10.1016/j.ijmecsci.2020.105482>
- [239] Liang ZY, Pharr GM (2022) Decoupling indentation size and strain rate effects during nanoindentation: a case study in tungsten. *J Mech Phys Solids* 165:104935. <https://doi.org/10.1016/j.jmps.2022.104935>
- [240] Cui L, Yu C-H, Jiang S, Sun X, Peng RL, Lundgren J-E, Moverare J (2022) A new approach for determining GND and SSD densities based on indentation size effect: an application to additive-manufactured Hastelloy X. *J Mater Sci Technol* 96:295–307. <https://doi.org/10.1016/j.jmst.2021.05.005>
- [241] Liu W, Chen L, Cheng Y, Yu L, Yi X, Gao H, Duan H (2019) Model of nanoindentation size effect incorporating the role of elastic deformation. *J Mech Phys Solids* 126:245–255. <https://doi.org/10.1016/j.jmps.2019.02.015>
- [242] Sudharshan Phani P, Oliver WC (2020) Critical examination of experimental data on strain bursts (pop-in) during spherical indentation. *J Mater Res* 35:1028–1036. <https://doi.org/10.1557/jmr.2019.416>
- [243] Weaver JS, Kalidindi SR (2016) Mechanical characterization of Ti–6Al–4V titanium alloy at multiple length scales using spherical indentation stress-strain measurements. *Mater Des* 111:463–472. <https://doi.org/10.1016/j.matdes.2016.09.016>
- [244] Campbell CJ, Gill S (2019) An analytical model for the flat punch indentation size effect. *Int J Solids Struct* 171:81–91. <https://doi.org/10.1016/j.ijsolstr.2019.05.004>
- [245] Yu Z, Lin Z, Wei Y (2021) Closed-form functions of cross-scale indentation scaling relationships based on a strain gradient plasticity theory. *Philos Mag* 101:1305–1326. <https://doi.org/10.1080/14786435.2021.1897896>
- [246] Yin F, Hu S, Xu R, Han X, Qian D, Wei W, Hua L, Zhao K (2020) Strain rate sensitivity of the ultrastrong gradient nanocrystalline 316L stainless steel and its rate-dependent modeling at nanoscale. *Int J Plast* 129:102696. <https://doi.org/10.1016/j.ijplas.2020.102696>
- [247] dos Santos T, Srivastava A, Rodríguez-Martínez JA (2021) The combined effect of size, inertia and porosity on the indentation response of ductile materials. *Mech Mater* 153:103674. <https://doi.org/10.1016/j.mechmat.2020.103674>
- [248] Marteau J, Jourani A, Bigerelle M (2020) Determination of an objective criterion for the assessment of the feasibility of an instrumented indentation test on rough surfaces. *Materials* 13:1589. <https://doi.org/10.3390/ma13071589>
- [249] Marimuthu KP, Park S, Jeong U, Lee H (2021) Dual flat-spherical indentation for extracting elastic–plastic properties from rough metallic surfaces. *Mater Des* 208:109909. <https://doi.org/10.1016/j.matdes.2021.109909>
- [250] Sudharshan Phani P, Oliver WC (2019) A critical assessment of the effect of indentation spacing on the

- measurement of hardness and modulus using instrumented indentation testing. *Mater Des* 164:107563. <https://doi.org/10.1016/j.matdes.2018.107563>
- [251] Weng P, Yin X, Hu W, Yuan H, Chen C, Ding H, Yu B, Xie W, Jiang L, Wang H (2021) Piecewise linear deformation characteristics and a contact model for elastic-plastic indentation considering indenter elasticity. *Tribol Int* 162:107114. <https://doi.org/10.1016/j.triboint.2021.107114>
- [252] Shahjahan NB, Hu Z (2017) Effects of angular misalignment on material property characterization by nanoindentation with a cylindrical flat-tip indenter. *J Mater Res* 32:1456–1465. <https://doi.org/10.1557/jmr.2016.478>
- [253] Zhang Y, Jiang C, Yang Q, Zhang Y, Tian S, Yang Y, Jiang H (2022) Orientation behavior in TRC-ZA21 magnesium alloy with fine grain size during nano-indentation process. *Mater Sci Eng A-Struct* 15:143252. <https://doi.org/10.1016/j.msea.2022.143252>
- [254] Zhang T, Guo J, Wang W (2021) A strain-pattern-based spherical indentation method for simultaneous uniaxial tensile residual stress and flow property determination. *J Strain Anal Eng Des* 56:50–64. <https://doi.org/10.1177/0309324720921305>
- [255] Sreepriya T, Mythili R, Prasad Reddy GV (2022) Correlation between microstructure and nanomechanical properties of 9Cr–1Mo ferritic martensitic steel through instrumented indentation technique. *Mater Sci Eng A Struct* 840:142985. <https://doi.org/10.1016/j.msea.2022.142985>
- [256] Song Y, Hua L, Chu D, Lan J (2012) Characterization of the inhomogeneous constitutive properties of laser welding beams by the micro-Vickers hardness test and the rule of mixture. *Mater Des* 37:19–27. <https://doi.org/10.1016/j.matdes.2011.12.029>
- [257] Wu S, Xu T, Song M, Guan K (2016) Mechanical properties characterisation of welded joint of austenitic stainless steel using instrumented indentation technique. *Mater High Temp* 33:270–275. <https://doi.org/10.1080/09603409.2016.1187463>
- [258] Pham T-H, Kim S-E (2017) Characteristics of microstructural phases relevant to the mechanical properties in structural steel weld zone studied by using indentation. *Constr Build Mater* 155:176–186. <https://doi.org/10.1016/j.conbuildmat.2017.08.033>
- [259] Yonezu A, Akimoto H, Fujisawa S, Chen X (2013) Spherical indentation method for measuring local mechanical properties of welded stainless steel at high temperature. *Mater Des* 52:812–820. <https://doi.org/10.1016/j.matdes.2013.06.015>
- [260] Awale DD, Vijayanand VD, Ballal AR, Thawre MM, Ganesh Kumar J, Prasad Reddy GV (2021) Evaluation of tensile properties of various regions of creep exposed dissimilar weld joint using miniature specimen testing. *Eng Fail Anal* 120:105079. <https://doi.org/10.1016/j.engfailanal.2020.105079>
- [261] Mohamadizadeh A, Biro E, Worswick M (2022) Failure characterization and meso-scale damage modeling of spot welds in hot-stamped automotive steels using a hardness-mapping approach. *Eng Fract Mech* 268:108506. <https://doi.org/10.1016/j.engfractmech.2022.108506>
- [262] Campbell JE, Zhang H, Burley M, Gee M, Fry AT, Dean J, Clyne TW (2021) A critical appraisal of the instrumented indentation technique and profilometry-based inverse finite element method indentation plastometry for obtaining stress–strain curves. *Adv Eng Mater* 23:2001496. <https://doi.org/10.1002/adem.202001496>
- [263] Sun Y, Peng G, Hu Y, Dou G, Chen P, Zhang T (2021) Spherical indentation model for evaluating the elastic properties of the shell of microsphere with core–shell structure. *Int J Solids Struct* 230–231:111159. <https://doi.org/10.1016/j.ijsolstr.2021.111159>
- [264] Sánchez-Ávila D, Barea R, Martínez E, Blasco JR, Portolés L, Carreño F (2018) Determination of the instantaneous strain rate during small punch testing of 316 L stainless steel. *Int J Mech Sci* 149:93–100. <https://doi.org/10.1016/j.ijmecsci.2018.09.042>

Publisher's Note Springer Nature remains neutral with regard to jurisdictional claims in published maps and institutional affiliations.

Springer Nature or its licensor (e.g. a society or other partner) holds exclusive rights to this article under a publishing agreement with the author(s) or other rightsholder(s); author self-archiving of the accepted manuscript version of this article is solely governed by the terms of such publishing agreement and applicable law.